Remote sensing the spatial and temporal structure of magnetopause and magnetotail reconnection from the ionosphere

G. Chisham,[1] M. P. Freeman,[1] G. A. Abel,[1] M. M. Lam,[1] M. Pinnock,[1] I. J. Coleman,[1] S. E. Milan,[2] M. Lester,[2] W. A. Bristow,[3] R. A. Greenwald,[4] G. J. Sofko,[5] J.-P. Villain,[6]

G.Chisham, M.P.Freeman, G.A.Abel, M.M.Lam, M. Pinnock, I.J.Coleman, British Antarctic Survey, Natural Environment Research Council, High Cross, Madingley Road, Cambridge, CB3 0ET, United Kingdom. (gchi@bas.ac.uk, mpf@bas.ac.uk, gaa@bas.ac.uk, mml@bas.ac.uk, mpi@bas.ac.uk)

S.E.Milan, M.Lester, Department of Physics and Astronomy, University of Leicester, Leicester, LE1 7RH, United Kingdom.

W.A.Bristow, UAF Geophysical Institute, 903 Koyukuk Drive, Fairbanks, Alaska 99775, USA.

R.A.Greenwald, Applied Physics Laboratory, Johns Hopkins University, Laurel, MD 20723, USA.

G.J.Sofko, University of Saskatchewan, 116 Science Place, Saskatoon, Saskatchewan, S7N 5E2, Canada.

J.-P.Villain, LPCE/CNRS, 3A, Avenue de la recherche Scientifique, Orleans, 45071, France.

[1]British Antarctic Survey, Natural

Abstract. Magnetic reconnection is the most significant process that results in the transport of magnetised plasma into, and out of, the Earth's magnetosphere-ionosphere system. There is also compelling observational evidence that it plays a major role in the dynamics of the solar corona, and it may also be

---

Environment Research Council, High Cross, Madingley Road, Cambridge, CB3 0ET, United Kingdom.

[2]Department of Physics and Astronomy, University of Leicester, Leicester, LE1 7RH, United Kingdom.

[3]UAF Geophysical Institute, 903 Koyukuk Drive, Fairbanks, Alaska 99775, USA.

[4]Applied Physics Laboratory, Johns Hopkins University, Laurel, MD 20723, USA.

[5]University of Saskatchewan, 116 Science Place, Saskatoon, Saskatchewan, S7N 5E2, Canada.

[6]LPCE/CNRS, 3A, Avenue de la recherche Scientifique, Orleans, 45071, France.

important for understanding cosmic rays, accretion disks, magnetic dynamos, and star formation. The Earth's magnetosphere and ionosphere are presently the most accessible natural plasma environments where magnetic reconnection and its consequences can be measured, either in situ, or by remote sensing. This paper presents a complete methodology for the remote sensing of magnetic reconnection in the magnetosphere from the ionosphere. This method combines measurements of ionospheric plasma convection and the ionospheric footprint of the reconnection separatrix. Techniques for measuring both the ionospheric plasma flow and the location and motion of the reconnection separatrix are reviewed, and the associated assumptions and uncertainties assessed, using new analyses where required. Application of the overall methodology is demonstrated by the study of a 2-hour interval from 26 December 2000 using a wide range of spacecraft and ground-based measurements of the northern hemisphere ionosphere. This example illustrates how spatial and temporal variations in the reconnection rate, as well as changes in the balance of magnetopause (dayside) and magnetotail (nightside) reconnection, can be routinely monitored, affording new opportunities for understanding the universal reconnection process and its influence on all aspects of space weather.

1. Introduction

It has been estimated that over 99.99% of the universe is made up of plasma - the fourth state of matter, composed of free ions and electrons. Despite its universal importance, our understanding of natural plasmas is limited by our ability to observe their behaviour and measure their properties. The most accessible natural plasma environment for study is the Earth's magnetosphere-ionosphere system. The Earth's magnetosphere is that region of near-Earth space which is permeated by the Earth's magnetic field. The plasma in the magnetosphere is controlled mainly by magnetic and electric forces that are much stronger here than gravity or the effect of collisions. The magnetosphere is embedded in the outflowing plasma of the solar corona, known as the solar wind, and its associated magnetic field, the interplanetary magnetic field (IMF). Because of the high conductivity of the solar wind and magnetospheric plasmas, their respective magnetic fields are effectively "frozen-in" to the plasma (like in a superconductor). The frozen-in nature of these two plasmas means that the solar wind cannot easily penetrate the Earth's magnetic field but is mostly deflected around it. This results in the distortion of the magnetosphere and the two plasmas end up being separated by a boundary, the magnetopause. The magnetopause is roughly bullet-shaped and extends to $\sim$10-12 Earth radii (R_E) on the dayside of the Earth, and stretches out into a long tail, the magnetotail, which extends to hundreds of R_E on the nightside of the Earth. However, the two plasma regions are not totally isolated as the process of magnetic reconnection allows the transmission of solar wind mass, energy, and momentum across the magnetopause, and into the magnetosphere.

Magnetic reconnection (or merging) is a physical process [*Priest and Forbes*, 2000] which involves a change in the connectivity of magnetic field lines (or magnetic flux) that facilitates the transfer of mass, momentum and energy. The resultant splicing together of different magnetic domains changes the overall topology of the magnetic field. If we consider a magnetic topology with antiparallel magnetic field lines frozen into two adjoining plasmas, where the plasma and magnetic field lines on both sides are moving toward each other, this results in a current sheet separating these regions, with a large change in the magnetic field across it. The frozen-in field approximation breaks down in this current sheet allowing magnetic field lines to diffuse across the plasma. This diffusion allows oppositely-directed magnetic fields to annihilate at certain points. This results in X-type configurations of the magnetic field, as shown in the schematic representation of a two-dimensional reconnection region in fig.1. Here, the magnetic field strength is zero at the centre of the X, termed the magnetic neutral point. The magnetic field lines forming the X, and passing through the neutral point, are called the separatrix. Plasma and magnetic field lines are transported toward the neutral point from either side as shown by the blue arrows in fig.1. Reconnection of the field lines occurs at the neutral point and the merged field lines, populated by a mixture of plasma from both regions, are expelled from the neutral point approximately perpendicular to their inflow direction. This process of magnetic reconnection is fundamental to the behaviour of the natural plasmas of many astrophysical environments. For example, solar flares, the largest explosion in the solar system, are caused by the reconnection of large systems of magnetic flux on the Sun, releasing in minutes the energy that has been stored in the solar magnetic field over a period of weeks to years. Reconnection is also important to the science of controlled nuclear fusion as it is one mechanism preventing the magnetic confinement of the fusion fuel.

At the Earth's magnetopause magnetic reconnection is the major process through which solar wind mass, energy and momentum are transferred from the solar wind into the magnetospheric system. Together with reconnection within the magnetotail, this drives a global circulation of plasma and magnetic flux within the magnetosphere and ionosphere [*Dungey*, 1961]. Figure 2 presents a schematic representation of the magnetosphere in the noon-midnight meridian plane which highlights the topology of the Earth's magnetic field and its connection to the IMF. Point N_1 marks an example location of a reconnection neutral point on the dayside magnetopause, with an IMF field line (marked 1) reconnecting with a geomagnetic field line (marked $1'$). Typically, the connectivity of geomagnetic field lines is of two types: Open - one end of the magnetic field line is connected to the Earth, the other to the IMF. Closed - both ends are connected to the Earth. Geomagnetic field line $1'$ represents the last closed field line in the dayside magnetosphere. As a result of the magnetopause reconnection two open field lines are created (marked 2 and $2'$) which are dragged by the solar wind flow to the nightside of the magnetosphere and into the magnetotail (to points 3 and $3'$). Here, the existence of the anti-parallel magnetic field configuration results in magnetotail reconnection (at neutral point N_2 in fig.2). In three dimensions, the reconnection X-points depicted as N_1 and N_2 in fig.2 are thought to extend along the magnetopause and magnetotail current sheets in lines known as X-lines. Figure 3 presents a 3-dimensional schematic representation of the magnetosphere which highlights these extended X-lines.

Accurate measurement of both the magnetopause and magnetotail reconnection rates, and an understanding of the factors that influence them has been a major scientific goal for many years. The reconnection rate (or equivalently the reconnection electric field) is defined as the rate of transfer of magnetic flux across unit length of the separatrix between the unreconnected and reconnected field lines. In the magnetospheric environment, important outstanding questions concerning reconnection, which can be addressed by reconnection rate measurements, include: Where is the typical location, and what is the typical extent (in both time and space), of both the magnetopause and magnetotail X-lines? How does the reconnection rate vary along these X-lines, and with time? How do these things change with changing interplanetary magnetic field and geomagnetic conditions?

The reconnection rate can be measured by spacecraft in the reconnecting current sheet, local to the neutral points, by measuring the electric field tangential to the reconnection X-line [*Sonnerup et al.*, 1981; *Lindqvist and Mozer*, 1990]. Such studies have shown evidence for a fast reconnection rate (inflow speed / Alfvén speed ~ 0.1) [*Priest and Forbes*, 2000]. However, it is generally difficult to measure the reconnection rate with satellites because it must be measured in the frame of reference of the separatrix, which is often in motion. Hence, such measurements are typically sparse in space and time, limited to the location and time of each spacecraft crossing of the current sheet.

More continuous and extensive measurements of reconnection in time and space can presently be achieved only by remotely sensing magnetic reconnection in the magnetosphere from the ionosphere. The ionosphere, located at altitudes of ~80-2000 km, forms the base of the magnetospheric plasma environment. It is the transition region from the fully-ionized magnetospheric plasma to the neutral atmosphere of the Earth. As can be seen in fig.3, the focussing effect of the Earth's dipole-like magnetic field projects reconnection signatures from the vast volume of the magnetosphere onto the relatively small area of the polar ionospheres, where they can be measured by ground- and space-based instruments. Hence, the ionospheric perspective is immensely valuable as a window to the huge outer magnetosphere and the reconnection processes occurring there.

In simple quasi-steady-state reconnection scenarios for different IMF orientations [*Dungey*, 1961, 1963; *Russell*, 1972; *Cowley*, 1981], and in the absence of other (e.g., viscous) transport processes [*Axford and Hines*, 1961], the total globally-integrated reconnection rate is equal to the maximum electric potential difference across the polar ionosphere. This can be measured every ∼100 min by low-altitude polar-orbiting satellites [*Reiff et al.*, 1981] or at higher cadence by ground-based radar and magnetometer networks [*Ruohoniemi and Baker*, 1998; *Richmond and Kamide*, 1988]. Such studies have investigated the functional dependence of the integrated reconnection rate on the relative orientation of the reconnecting magnetic fields [*Reiff et al.*, 1981; *Freeman et al.*, 1993].

More generally, imbalance of the integrated reconnection rates at the magnetopause and in the magnetotail results in a change in the relative proportions of open and closed magnetic flux [*Siscoe and Huang*, 1985; *Cowley and Lockwood*, 1992]. Thus, for unbalanced reconnection, the difference in the two integrated reconnection rates can be measured from the rate of change of polar cap area (the area of incompressible open magnetic flux that threads the polar ionospheres). Estimates of both the magnetopause and magnetotail reconnection rates can then be made whenever one or the other reconnection rate can be estimated [*Lewis et al.*, 1998], or is negligible [*Milan et al.*, 2003], or by summing the difference measurement with an estimate of the average of the two reconnection rates given by the cross-polar cap potential [*Cowley and Lockwood*, 1992]. Such studies have revealed and quantified the variation of global magnetopause and magnetotail reconnection through the substorm cycle [*Milan et al.*, 2007].

On shorter time scales, local reconnection rates have been inferred from low-altitude spacecraft observations of the dispersion of ions from the reconnection site precipitating into the ionosphere on newly-opened magnetic field lines [*Lockwood and Smith*, 1992]. These observations provide a temporal profile of the reconnection rate at a single location for the duration of the satellite pass ($\sim$10 min). Such studies show the reconnection rate to vary on timescales of minutes, as suggested by the in-situ observation of flux transfer events (instances of transient reconnection) at the magnetopause [*Russell and Elphic*, 1978].

Most generally, the reconnection rate is measured from the ionosphere by first detecting the ionospheric projections of regions of different magnetic connectivity (e.g., open and closed magnetospheric field lines) and then measuring the transport of magnetic flux between them. The reconnection rate equates to the component of the ionospheric convection electric field tangential to the ionospheric projection of the reconnection separatrix, in the frame of the reconnection separatrix. Hence, in a ground-based measurement frame, contributions can arise from (1) plasma convecting across the separatrix, and (2) movement of the separatrix in the measurement frame. As shown schematically in fig.3, the reconnection separatrix (yellow and green shaded areas) maps down magnetic field lines from the in-situ reconnection X-lines (bold blue lines in space) to regions in the polar ionospheres termed “merging lines” (bold blue lines in the ionosphere). The different magnetic field topologies in the two regions either side of the separatrix give rise to different plasma properties in each region, which can be detected at the ionospheric footprints. During southward IMF conditions, when magnetopause reconnection occurs preferentially on the low-latitude magnetopause (as in figs.2 and 3), the dayside merging line is co-located with the ionospheric projection of the open-closed magnetic field line boundary (OCB), alternatively termed the polar cap boundary. During strong northward IMF conditions, when reconnection occurs at high latitudes on the magnetotail lobe magnetopause, the reconnection separatrix is typically located some distance poleward of the OCB, within the polar cap, at the point where the lobe magnetopause maps into the ionosphere. On the nightside of the Earth the merging line associated with the most-distant magnetotail X-line is always co-located with the OCB. Reconnection is also thought to occur Earthward of this far-tail X-line (at a near-Earth neutral line) but there is not as yet a clear signature of the ionospheric projection of this X-line.

The first reconnection rate measurements of this type were made in the nightside ionosphere by *de la Beaujardière et al.* [1991] using Sondrestrom Incoherent Scatter Radar (ISR) measurements. Using a single meridional radar beam they measured the plasma velocity across the OCB in the OCB rest frame. The location of the OCB was estimated by identifying strong electron density gradients which occur at ionospheric E-region altitudes along the poleward boundary of the auroral oval. These are thought to be a good proxy for the OCB in the nightside ionosphere. *Blanchard et al.* [1996, 1997] later refined these measurements by locating the OCB using both E-region electron density measurements and 630 nm auroral emissions measured by ground-based optical instruments. They investigated how the magnetotail reconnection rate varied with magnetic local time, with variations in the IMF, and with substorm activity. Since then, a number of studies have used single radar beams to make single-point reconnection rate measurements of this type in both the dayside and nightside ionospheres [*Pinnock et al.*, 1999; *Blanchard et al.*, 2001; *Østgaard et al.*, 2005]. These studies have used a range of different techniques to determine the OCB location and motion. However, the employment of a single meridional radar beam in the above studies meant that no investigation could be made of spatial variations in the reconnection rate.

Baker et al. [1997] first measured the reconnection rate across an extended longitudinal region. They used the technique of L-shell fitting [*Ruohoniemi et al.*, 1989] to estimate two-dimensional ionospheric convection velocity vectors from line-of-sight velocity measurements made by a single radar of the Super Dual Auroral Radar Network (SuperDARN) [*Greenwald et al.*, 1995; *Chisham et al.*, 2007]. They also used variations in the Doppler spectral width characteristics measured by the radar to estimate the OCB location. Since then, the advent of large networks of ionospheric radars which can measure the plasma convection velocity over large regions of the ionosphere has made extensive measurements of the reconnection rate a reality. Recent studies [*Pinnock et al.*, 2003; *Milan et al.*, 2003; *Chisham et al.*, 2004b; *Hubert et al.*, 2006; *Imber et al.*, 2006] have employed the technique of SuperDARN global convection mapping to measure the convection velocity across large regions of the polar ionospheres for a range of IMF conditions. Combined with measurements of the location and motion of the ionospheric footprint of the reconnection separatrix from a range of different instrumentation, these studies have illustrated that the magnetopause reconnection rate not only varies with time but also with longitudinal location along the merging line. The magnetotail reconnection rate has also been studied in a similar way [*Lam et al.*, 2006; *Hubert et al.*, 2006].

The purpose of this paper is to build on these previous studies and to present a standard methodology for reconnection rate determination which can be easily implemented. To this end we:

(1) Set out in full a complete methodology for remote sensing of the reconnection rate.

(2) Review the techniques for determining the ionospheric convection velocity field and the ionospheric projection of the reconnection separatrix.

(3) Highlight and discuss problems and uncertainties concerning the methodology and techniques.

(4) Present an example of a global application of this methodology.

2. Methodology for estimating the reconnection rate

In this section we outline mathematically the methodology for determining reconnection rates using ionospheric measurements. We also review the instrumentation and analysis techniques used to make these ionospheric measurements. The application of many of these techniques is described by considering a 2-hour interval of data from 26 December 2000. The results of the reconnection rate analysis using the combined data sets from this interval are presented in section 3.

2.1. Theory

2.1.1. General formulation

The principle of remote measurement of the reconnection electric field was first presented by *Vasyliunas* [1984] who argued that the potential variation along the ionospheric projection of the reconnection separatrix (the merging line) related directly to that along the in-situ reconnection X-line. The reconnection electric field in the ionosphere equates to the component of the ionospheric convection electric field that is directed tangential to the ionospheric projection of the reconnection separatrix, in the frame of the separatrix. This equates to the rate of flux transfer across the reconnection separatrix, assuming that the magnetic field is frozen in to the plasma. It is assumed that the plasma flow in the polar ionosphere is dominated by the convection electric field and that the convection velocity field is divergence-free.

The reconnection rate, or electric field (E_{rec}), in the ionosphere at any point s along the reconnection separatrix at a time t can be written

$$E_{rec}(s,t) = \mathbf{E}'(s,t) \cdot \hat{\mathbf{T}}(s,t) \tag{1}$$

where $\mathbf{E}'(s,t)$ is the convection electric field at the separatrix, in the frame of the separatrix, and

$$\hat{\mathbf{T}}(s,t) = \frac{d\mathbf{P}(s,t)}{ds} \tag{2}$$

represents the tangent to the separatrix, where $\mathbf{P}(s,t)$ describes the location of the separatrix.

We can relate the convection electric field to the ionospheric convection velocity field if we assume the ideal magnetohydrodynamic approximation of Ohm's law

$$\mathbf{E}'(s,t) = -(\mathbf{V}'(s,t) \times \mathbf{B}(s)) \tag{3}$$

where $\mathbf{V}'(s,t)$ is the convection velocity at locations along the separatrix, in the frame of the separatrix (a one-dimensional path through the convection velocity field $\mathbf{V}'(\mathbf{x},t)$), and $\mathbf{B}(s) = B_z(s)\hat{\mathbf{z}}$ is the magnetic field (approximated as being vertical and time invariant).

The normal to the separatrix at a fixed ionospheric height can be written as,

$$\hat{\mathbf{N}}(s,t) = -(\hat{\mathbf{z}} \times \hat{\mathbf{T}}(s,t)) \tag{4}$$

and hence, combining (1), (3), and (4), the reconnection electric field, (1), can be rewritten as,

$$E_{rec}(s,t) = B_z(s)\left(\mathbf{V}'(s,t) \cdot \hat{\mathbf{N}}(s,t)\right) \tag{5}$$

The ionospheric convection velocity is not typically measured in the frame of the separatrix and hence we need to convert convection velocity measurements $\mathbf{V}(s,t)$ into this frame using the transformation,

$$\mathbf{V}'(s,t) = \mathbf{V}(s,t) - \frac{d\mathbf{P}(s,t)}{dt} \tag{6}$$

By combining (5) and (6) we can write the reconnection electric field as,

$$E_{rec}(s,t) = B_z(s)\left[\left(\mathbf{V}(s,t) - \frac{d\mathbf{P}(s,t)}{dt}\right) \cdot \hat{\mathbf{N}}(s,t)\right] \tag{7}$$

The total rate of flux transfer $(dF_{12}(t)/dt)$ along a merging line connecting points P_1 and P_2 is given by the integrated reconnection rate, or reconnection voltage $(\phi_{12}(t))$, which is determined by integrating the reconnection electric field along this merging line.

$$\begin{aligned}
\phi_{12}(t) &= \frac{dF_{12}(t)}{dt} \\
&= \int_{P_1}^{P_2} E_{rec}(s,t)\, ds \\
&= \int_{P_1}^{P_2} B_z(s)\left[\left(\mathbf{V}(s,t) - \frac{d\mathbf{P}(s,t)}{dt}\right) \cdot \hat{\mathbf{N}}(s,t)\right] ds
\end{aligned} \tag{8}$$

Typically, reconnection at the magnetopause increases open magnetic flux whereas reconnection in the magnetotail decreases open flux. Consequently the total globally-integrated reconnection rate in the magnetospheric system is given by the rate of change of open magnetic flux in the polar cap

$$\frac{dF_{pc}}{dt} = B_i \frac{dA_{pc}}{dt} = \phi_d + \phi_n \tag{9}$$

where ϕ_d and ϕ_n are the total reconnection voltages along the magnetopause and magnetotail X-lines, respectively, and A_{pc} is the area of open flux in the ionosphere. Measuring the reconnection rate from the ionosphere offers the advantages that A_{pc} is minimized and B_i is approximately constant and hence can be described by a static empirical model. Thus, by measuring changes in polar cap area, the measurement of either of the magnetopause or magnetotail reconnection voltages allows estimation of the other [*Milan et al.*, 2003].

2.1.2. Discrete formulation

Actual measurements of the convection velocity ($\mathbf{V}$) and the reconnection separatrix position in the ionosphere ($\mathbf{P}$) typically comprise sparse discrete observations, rather than continuous functions. Consequently, for practical purposes we rewrite (7) in a discrete form as,

$$E_{rec_i}(t) = B_{z_i} \left[(\mathbf{V}_i(t) - \mathbf{V}_{\mathbf{P}_i}(t)) \cdot \hat{\mathbf{N}}_i(t) \right] \tag{10}$$

where subscript i refers to a discrete velocity vector measurement and where the motion of the separatrix has been simplified as $\mathbf{V}_{\mathbf{P}_i}$ (the meridional component of the separatrix velocity at the location of velocity vector i). For ease of calculation we rewrite this as,

$$E_{rec_i}(t) = B_{z_i} \left[|\mathbf{V}_i(t)| \cos\theta_i(t) - |\mathbf{V}_{\mathbf{P}_i}(t)| \cos\alpha_i(t) \right] \tag{11}$$

where θ_i is the angle between the velocity vector and the normal to the separatrix and α_i is the angle between the meridional direction and the normal to the separatrix. Hence, estimates of the reconnection rate require measurements of the vertical magnetic field strength, the separatrix location and motion, and the convection velocity. The magnetic field strength varies little in the incompressible ionosphere and so values from the Altitude-Adjusted Corrected Geomagnetic (AACGM) field model [*Baker and Wing*, 1989] can be assumed. The AACGM model is also used as the geomagnetic coordinate system in this analysis.

Generally, our discrete measured velocity vectors will not be co-located with the measured separatrix location. Hence, we consider velocity vectors close to the separatrix to be the best estimate of the velocity field at the separatrix. Typically, those within half the latitudinal resolution of the velocity measurements are most suitable. Fig.4 presents a basic schematic representation of the scenario at each discrete measurement point i. Figure 4a presents an example scenario of the actual measured quantities. We have suitable velocity vectors $\mathbf{V}_i = \mathbf{V}(\lambda_i, \phi_i)$ at N discrete locations with AACGM latitude λ_i and AACGM longitude ϕ_i $(i = 1...N)$ and separatrix identifications $\mathbf{P}_j = \mathbf{P}(\lambda_j, \phi_j)$ at M discrete positions with AACGM latitude λ_j and AACGM longitude ϕ_j $(j = 1...M)$. Figure 4b shows the derived quantities that are used as input to equation (11) for the same example as in fig.4a. For each velocity vector we assume that the measured velocity is a good approximation for the velocity at the separatrix at the same AACGM longitude. $\mathbf{P}_i$ is an estimate of the separatrix position at AACGM longitude ϕ_i, the latitude of which can be approximated by the linear interpolation of neighbouring separatrix measurements $(\lambda_{j_1}, \phi_{j_1})$ and $(\lambda_{j_2}, \phi_{j_2})$,

$$\lambda(\mathbf{P}_i) = \lambda_{j_1} + \left(\frac{\lambda_{j_2} - \lambda_{j_1}}{\phi_{j_2} - \phi_{j_1}}\right)(\phi_i - \phi_{j_1}) \tag{12}$$

If the discrete separatrix points are not too far apart then we can assume a locally linear approximation. Therefore, the angle $\alpha_i = \alpha(\mathbf{P}_i)$ between the normal to the separatrix and the meridional direction can be given as,

$$\alpha_i = \tan^{-1}\left[\frac{\lambda_{j_2} - \lambda_{j_1}}{(\phi_{j_2} - \phi_{j_1})\cos\lambda_{j_2}}\right]. \tag{13}$$

Alternatively, $\lambda(\mathbf{P}_i)$ and α_i can be estimated by a higher order method (see section 2.3.6).

The angle between the velocity vector $\mathbf{V}_i$ and the meridian direction is given by $\theta_{\mathbf{V}_i} = \theta_{\mathbf{V}}(\lambda_i, \phi_i)$. Hence, the angle between the velocity vector and the normal to the separatrix is given by,

$$\theta_i = \theta_{\mathbf{V}_i} - \alpha_i \tag{14}$$

We assume for simplicity that the separatrix motion in the ionosphere is purely latitudinal and hence the magnitude of the separatrix velocity at AACGM longitude ϕ_i is given by,

$$|\mathbf{V}_{\mathbf{P}_i}(t)| = \frac{(R_E + h)\,[\lambda(\mathbf{P}_i(t)) - \lambda(\mathbf{P}_i(t - \Delta t))]}{\Delta t} \tag{15}$$

where R_E is the radius of the Earth, h is the altitude of the observations, and Δt is the time between successive separatrix estimates.

Entering single point measurements into (11) allows us to make localised estimates of the reconnection electric field [*Pinnock et al.*, 1999; *Blanchard et al.*, 2001]. However, if we wish to determine the spatiotemporal structure of the electric field or make an estimate of the reconnection voltage along a merging line, we need to make as many measurements as possible along the merging line. If we assume N_{vec} discrete velocity vector measurements along a merging line, the total rate of flux transfer, or reconnection voltage, for that merging line can be estimated from,

$$\phi_{rec}(t) = \sum_{i=1}^{N_{vec}} E_{rec_i}(t)\,\Delta s_i(t) \tag{16}$$

where $\Delta s_i(t)$ represents the length of the separatrix portion at measurement location i, which for closely-spaced measurements can be approximated by,

$$\Delta s_i(t) \approx \left(\frac{|\mathbf{P}_{i+1}(t) - \mathbf{P}_{i-1}(t)|}{2} \right) \tag{17}$$

2.1.3. Error analysis

In order to gain a quantitative feel for reconnection rate estimates we need to have an appreciation of the uncertainties in the measured quantities. We can estimate the uncertainty, or error, in a single measurement of the reconnection electric field at measurement point i as,

$$\varepsilon\langle E_{rec_i}(t)\rangle \approx B_{z_i} \left(\varepsilon\langle|\mathbf{V}_i(t)|\cos\theta_i(t)\rangle^2 + \varepsilon\langle|\mathbf{V}_{\mathbf{P}_i}(t)|\cos\alpha_i(t)\rangle^2 \right)^{\frac{1}{2}} \tag{18}$$

where $\varepsilon\langle x\rangle$ represents the uncertainty in the measurement of parameter x. (This representation assumes that the uncertainty in the magnetic field ($\varepsilon\langle B_{z_i}\rangle$) is negligible.) This uncertainty should only be viewed as an estimate as strictly the formulation requires that $|\mathbf{V}_i(t)|\cos\theta_i(t)$ and $|\mathbf{V}_{\mathbf{P}_i}(t)|\cos\alpha_i(t)$ are independent and uncorrelated. This is not strictly true since both have some dependence on the normal to the separatrix ($\hat{\mathbf{N}}_i(t)$). From (18), the uncertainty in $E_{rec_i}(t)$ is dependent on: (1) $\varepsilon\langle|\mathbf{V}_i(t)|\cos\theta_i(t)\rangle$, the uncertainty in the convection velocity measurement, and (2) $\varepsilon\langle|\mathbf{V}_{\mathbf{P}_i}(t)|\cos\alpha_i(t)\rangle$, the uncertainty in the measurement of the separatrix motion.

The uncertainty in the convection velocity measurement can be approximated as,

$$\varepsilon\langle|\mathbf{V}_i(t)|\cos\theta_i(t)\rangle \approx \left(\cos^2\theta_i(t)\varepsilon\langle|\mathbf{V}_i(t)|\rangle^2 + |\mathbf{V}_i(t)|^2 \sin^2\theta_i(t)\varepsilon\langle\theta_i(t)\rangle^2 \right)^{\frac{1}{2}} \tag{19}$$

which again assumes that the uncertainties in $|\mathbf{V}_i(t)|$ and $\theta_i(t)$ are independent and uncorrelated. The uncertainties in the velocity magnitude ($\varepsilon\langle|\mathbf{V}_i(t)|\rangle$) and in the angle that the velocity vector makes with the separatrix normal ($\varepsilon\langle\theta_i(t)\rangle$) are inherently difficult to estimate and depend largely on the technique being employed to determine the convection velocity. However, it is possible to simplify our uncertainty estimates to allow a rough estimate of the level of uncertainty. If we assume that the uncertainty in the velocity magnitude is proportional to the magnitude ($\varepsilon\langle|\mathbf{V}_i(t)|\rangle = a_1|\mathbf{V}_i(t)|$, where a_1 is a constant), and that the uncertainty in the angle can be given by $\varepsilon\langle\theta_i(t)\rangle = a_2$ (where a_2 is in radians), then the uncertainty in the convection velocity measurement can be rewritten as,

$$\varepsilon\langle|\mathbf{V}_i(t)|\cos\theta_i(t)\rangle \approx |\mathbf{V}_i(t)|\left[a_1^2\cos^2\theta_i(t) + a_2^2\sin^2\theta_i(t)\right]^{\frac{1}{2}}. \tag{20}$$

To illustrate the range of possible uncertainties we consider the limits of equation (20): If $\theta_i(t) = 0°$ (the velocity vector is perpendicular to the separatrix), equation (20) reduces to,

$$\varepsilon\langle|\mathbf{V}_i(t)|\cos\theta_i(t)\rangle \approx a_1|\mathbf{V}_i(t)| \tag{21}$$

which implies that the uncertainty relates solely to the uncertainty in the velocity vector magnitude. If $\theta_i(t) = 90°$ (the velocity vector is parallel to the separatrix), this reduces to,

$$\varepsilon\langle|\mathbf{V}_i(t)|\cos\theta_i(t)\rangle \approx a_2|\mathbf{V}_i(t)| \tag{22}$$

which implies that the uncertainty relates solely to the uncertainty in the direction of the velocity vector.

The uncertainty in the separatrix motion at a measurement point, i, can be given by,

$$\varepsilon\langle|\mathbf{V}_{\mathbf{P}_i}(t)|\cos\alpha_i(t)\rangle \approx \left(\cos^2\alpha_i(t)\varepsilon\langle|\mathbf{V}_{\mathbf{P}_i}(t)|\rangle^2 + |\mathbf{V}_{\mathbf{P}_i}(t)|^2\sin^2\alpha_i(t)\varepsilon\langle\alpha_i(t)\rangle^2\right)^{\frac{1}{2}} \tag{23}$$

Hence, this uncertainty can be written in terms of the uncertainty in the difference in the temporal separatrix positions, and the uncertainty in the angle that the separatrix normal makes with the meridional direction. If we make the assumption that both $\alpha_i(t)$ and $\varepsilon\langle\alpha_i(t)\rangle$ are likely to be small (i.e., the separatrix normal will be aligned close to the the meridional direction and is likely to be well defined), then we can simplify (23) to,

$$\varepsilon\langle|\mathbf{V}_{\mathbf{P}_i}(t)|\cos\alpha_i(t)\rangle \approx \varepsilon\langle|\mathbf{V}_{\mathbf{P}_i}(t)|\rangle = \frac{1}{\Delta t}(R_E + h)\varepsilon\langle\lambda(\mathbf{P}_i(t)) - \lambda(\mathbf{P}_i(t-\Delta t))\rangle \quad (24)$$

Hence, the uncertainty depends heavily on Δt. As the temporal resolution of the measurements increases (Δt decreases) the uncertainty in the separatrix motion will increase. Hence, increasing the time resolution of measurements requires an increase in the accuracy of the separatrix measurements to keep the level of uncertainty low. The uncertainty in the difference in the separatrix positions is heavily dependent on the spatial resolution of the measurement technique.

2.2. Measuring the ionospheric convection velocity field

A complete picture of the reconnection scenario requires continuous and extensive measurement of the ionospheric convection velocity in space and time. At present, there are two techniques in regular use which can provide such a picture of the convection velocity field across the complete polar ionosphere.

(1) The Assimilative Mapping of Ionospheric Electrodynamics (AMIE) technique. AMIE is an inversion technique used to derive the mathematical fields of physical variables for the global ionosphere at a given time from spatially irregular measurements of these variables or related quantities [*Richmond and Kamide*, 1988]. The field variables are the electrostatic potential, electric field, height-integrated current density and conductivity, and field-aligned current density at a given height. Measurements are made by magnetometers on the ground and on low-altitude satellites, ground-based radars, plasma drift

and particle detectors on low-altitude satellites, and optical instruments on the ground and on satellites.

(2) The SuperDARN Global Convection Mapping (or Map Potential) technique. SuperDARN global convection maps are produced by fitting line-of-sight velocity information measured by the SuperDARN radars to an expansion of an electrostatic potential function expressed in terms of spherical harmonics [*Ruohoniemi and Baker*, 1998]. This method uses all of the available line-of-sight velocity data from the SuperDARN HF radar network. It can also accept ion drift velocity data from low-altitude spacecraft as input.

Lu et al. [2001] showed that convection maps derived using the AMIE and SuperDARN global convection mapping techniques, using the same radar data as input, were nearly identical over areas of extensive radar coverage. However, significant differences arose where data were sparse or absent because different statistical models were used by each technique to constrain the global solution in these regions. Furthermore, they derived AMIE convection maps using SuperDARN radar data and magnetometer data separately, the coverage of which was concentrated in different regions. These also showed significant differences in regions where data were sparse or absent in one or other data set and values of the cross-polar cap potential that differed by $\sim$65%. We are aware of only two studies in which the AMIE technique has been used to identify the reconnection separatrix [*Taylor et al.*, 1996] and the flow across it [*Lu et al.*, 1995] whereas SuperDARN global convection mapping has regularly been used for these purposes [*Pinnock et al.*, 2003; *Milan et al.*, 2003; *Chisham et al.*, 2004b; *Hubert et al.*, 2006].

For the event study in this paper we use the SuperDARN global convection mapping technique to provide our estimate of the ionospheric convection velocity field, because it is specifically designed to measure the convection electric field. Full details of the technique (and the data-preprocessing it requires) can be found in *Ruohoniemi and Baker* [1998], *Shepherd and Ruohoniemi* [2000], *Chisham and Pinnock* [2002], and *Chisham et al.* [2002]. The technique provides an estimate of the convection potential ($\Phi(\lambda, \phi)$) and electric field ($E = -\nabla\Phi(\lambda, \phi)$) across the whole polar ionosphere in the Earth's rest frame and can be used to study large-scale characteristics (e.g., the cross-polar cap potential [*Shepherd and Ruohoniemi*, 2000]) or mesoscale features (e.g., flow vortices, convection reversal boundaries [*Huang et al.*, 2000]). The scale of resolvable structure is limited by the order of the spherical harmonic fit and the grid cell size of the radar measurements. In practice, the technique is generally not suitable for small-scale structure ($<\sim$ 100 km - the basic grid cell size). The analytical solution for the convection electric field can be used to determine the reconnection rate at all points on the merging lines [*Milan et al.*, 2003; *Hubert et al.*, 2006]. However, the accuracy of these estimates is likely to be poor in regions with no SuperDARN data. We recommend that reconnection rates are only determined in regions where SuperDARN data have contributed to the global convection electric field solution.

Whereas a solution is provided for the convection electric field across the whole polar ionosphere, velocity vectors are only determined in regions where SuperDARN backscatter have contributed to the fitting process. At these locations, the global convection mapping technique provides two alternative methods for determining velocity vectors, which have been termed 'fit' and 'true' vectors.

'Fit' velocity vectors represent the $\mathbf{E} \times \mathbf{B}$ drift velocities of the convection electric field solution at each grid cell (λ_i, ϕ_i) which contributed line-of-sight velocity information to the mapping process and are hence given by

$$\mathbf{V}_{fit}(\lambda_i, \phi_i) = \frac{-\nabla\Phi(\lambda_i, \phi_i) \times \mathbf{B}(\lambda_i, \phi_i)}{|\mathbf{B}(\lambda_i, \phi_i)|^2}. \tag{25}$$

The fit vectors are always tangential to equipotentials of the convection electric field solution and are divergence-free. However, the fit vector is often inconsistent with the corresponding line-of-sight velocity measured by radar r in that grid cell ($\mathbf{V}_{los}(\lambda_i, \phi_i, r)$), as the fit vector is determined by the global solution and not solely the local observations. The correlation between the two becomes better as the order of the spherical harmonic fit is increased and more of the mesoscale variations in the velocity measurements can be fitted to.

'True' velocity vectors represent a combination of the line-of-sight velocity measured at each grid cell with the component of the fit velocity vector which is perpendicular to the line-of-sight direction and are hence given by

$$\mathbf{V}_{true}(\lambda_i, \phi_i, r) = |\mathbf{V}_{fit}(\lambda_i, \phi_i) \times \hat{\mathbf{V}}_{los}(\lambda_i, \phi_i, r)| \left(\hat{\mathbf{V}}_{los}(\lambda_i, \phi_i, r) \times \hat{\mathbf{z}}\right) + \mathbf{V}_{los}(\lambda_i, \phi_i, r) \tag{26}$$

The true vectors typically provide a better mesoscale representation of the ionospheric convection flows [*Chisham et al.*, 2002; *Provan et al.*, 2002]. For this reason, some previous studies which have used SuperDARN global convection mapping to determine the reconnection electric field [*Pinnock et al.*, 2003; *Chisham et al.*, 2004b] have used true vectors, and we will do so here. However, the true vector velocity field is not guaranteed to be divergence free and there is also the possibility of an ambiguity in the true vector magnitude and direction if a grid cell contains line-of-sight velocity information from more than one SuperDARN radar. As the goodness of the spherical harmonic fit increases, the true vectors become increasingly closer to agreement with the fit vectors.

Figure 5 presents the northern hemisphere convection map for a 1-minute interval (2017–2018 UT) on 26 December 2000 determined using the SuperDARN global convection mapping technique. The velocity vectors are true vectors, with a length proportional to the velocity magnitude. The equipotential contours of the solution ($\Phi(\lambda, \phi)$) which results from the spherical harmonic fitting are shown by the dashed (morning convection cell) and dotted (afternoon convection cell) contour lines. The spatial coverage of the vectors highlights the region of the convection map where actual SuperDARN data exist. The equipotential contours in regions where no data exist are heavily influenced by data from the statistical model of *Ruohoniemi and Greenwald* [1996] and hence only provide a statistical estimate of the true convection in these regions. However, the model does serve to constrain the spherical harmonic fit to provide a realistic estimate of convection at the boundaries of the measured data set. In the example event studied in this paper we only estimate reconnection rates in regions where we have measured true velocity vectors.

The SuperDARN global convection mapping technique often provides an extensive representation of the convection electric field as shown in figure 5. However, uncertainties in the magnitude and direction of the velocity vectors are not readily expressed. There are a number of aspects of the technique which introduce uncertainty into the output (aside from the uncertainties in the input line-of-sight velocity values), as discussed below:

(1) Before processing the data for a particular interval, the line-of-sight velocities are generally median filtered, both spatially (across a $\sim$100 km square grid cell) and temporally (across three successive radar scans - $\sim$3-6 min) to increase the statistical significance of the output. Hence, localized or short bursts of strong flow on these scales can be par-

tially averaged away. This will ultimately lead to some smoothing of the spatial and temporal reconnection rate variations.

(2) The least-squares fitting is dependent on two user-selected parameters; (i) the order of the spherical harmonic fit, and (ii) the spatial region over which the fit is performed (primarily the low-latitude boundary of ionospheric convection). Variations in these fit parameters lead to differences in the final solution [*Ruohoniemi and Baker*, 1998; *Shepherd and Ruohoniemi*, 2000]. Higher order fits produce convection maps that better match the line-of-sight velocity input, but which have lower statistical significance.

(3) Pre-inspection of the data can be important if the determination of mesoscale features of convection is required. Care must be taken to ensure that all the backscatter being used in the convection mapping process has arisen from F-region irregularities moving under the influence of the convection electric field. Presently, some ground and E-region backscatter typically remain after default preprocessing of the SuperDARN data. This can increase the uncertainties in the reconnection rate calculations. These uncertainties can be reduced by careful inspection of the line-of-sight velocity data and by filtering the data in range gate-velocity space to remove non-F-region data before applying the mapping technique [*Chisham and Pinnock*, 2002] .

2.3. Identifying the location and motion of the reconnection separatrix

The ionospheric footprint of the reconnection separatrix (the merging line) is usually determined using well-established proxies. The reliability of these proxies is variable and is affected by IMF variations, geomagnetic conditions, and spatial location in the ionosphere. During intervals when reconnection is occurring on the lobe magnetopause, i.e., when the IMF is close to being northward directed (IMF $B_z > 0$; $B_y \sim 0$), the dayside merging line typically lies some distance poleward of the OCB, within the polar cap. In this paper we only consider intervals where reconnection is occurring on regions of the magnetopause sunward of the magnetospheric cusps (i.e., when the IMF is not strongly northward), and hence when the dayside merging line is co-located with the OCB [*Cowley and Lockwood*, 1992]. In the nightside ionosphere the reconnection separatrix for far-tail reconnection is always co-located with the OCB. Hence, for most conditions and locations we are trying to measure proxies for the OCB. The methodology presented here is still applicable to the estimation of reconnection rates away from the OCB (such as at the ionospheric footprint of lobe reconnection during northward IMF conditions [*Chisham et al.*, 2004b], or at the ionospheric footprint of the near-Earth neutral line in the tail), but the identification of the reconnection separatrix in these cases is less established, as will be discussed in section 4.

2.3.1. Particle precipitation boundaries

The high-latitude ionosphere, through its magnetic connection to the outer magnetosphere, provides an image of magnetospheric regions and boundaries and the physical processes occurring there. From numerous observations made by the DMSP low-altitude satellites, the energy spectra of precipitating ions and electrons have been categorised into different types. These types correspond to different plasma regions in the Earth's magnetosphere whose ionospheric footprints can consequently be identified in an objective way [*Newell et al.*, 1991; *Newell and Meng*, 1992; *Newell et al.*, 1996]. Some plasma regions are typically located on open magnetic field lines and others on closed [*Sotirelis and Newell*, 2000] and hence, one can use these low-altitude measurements to identify the OCB location. In the dayside ionosphere, the OCB is best identified by a transition between the precipitation regions typically thought to be associated with open (i.e., cusp, mantle, polar rain) and closed (i.e., central plasma sheet, boundary plasma sheet, low-latitude boundary layer) field lines [*Newell et al.*, 1991]. In the nightside ionosphere, the best OCB proxy is the b6 precipitation boundary [*Newell et al.*, 1996] which marks the poleward edge of the sub-visual drizzle region. As discussed earlier, there are times when the OCB is not co-located with the separatrix. In these cases the magnetopause reconnection separatrix can be identified by the high-energy edge of velocity dispersed ion precipitation [*Rosenbauer et al.*, 1975; *Hill and Reiff*, 1977; *Burch et al.*, 1980].

Relative to other ionospheric proxies, low-altitude spacecraft particle precipitation observations provide a more direct measurement of the reconnection separatrix in the ionosphere. However, they only provide limited point measurements of the boundary location as the spacecraft pass across each of the polar regions once in their orbits (typically ∼100-min for DMSP spacecraft). Nevertheless, as the most reliable boundary indicators they have an important role in calibrating other proxies, both in single event studies, and on a more statistical basis. The following sections discuss some of these large-scale statistical calibrations.

2.3.2. Auroral observations

When magnetospheric particles precipitate into the denser regions of the lower ionosphere they collide with other particles to give off light, causing the aurora. The intensity and wavelength of auroral emissions depends partially on the flux, energy and species of the precipitating particles, which is different on either side of the OCB as discussed above. These auroral emissions can be detected with both ground-based and space-based imagers. Observations of the aurora, particularly in the visible and ultraviolet (UV) frequency bands, provide information about the geographical distributions of the precipitating particles and their source regions.

Auroral observations are made from the ground using all-sky cameras and photometers. The altitude from which most auroral luminosity is emitted is ~110 km (the ionospheric E-region) [*Rees*, 1963], and therefore the greatest distance at which aurora can theoretically be observed (the viewing horizon) is slightly over 1000 km. In practice, the effects of landscape, vegetation, and optical effects at low elevation angles reduce this viewing horizon to ~300 km. Ground observations can achieve high spatial resolution at the zenith of the camera, but the resolution drops sharply towards the edges of the field-of-view. The temporal resolution of observations can be very high, though is typically ~1 min. Uncertainties in the altitude of the auroral emission can lead to inaccuracies in mapping the observations to a geographical grid, and these uncertainties increase away from the zenith. Ground-based cameras cannot make observations in inclement weather, nor when the sun is up or during full moon. Consequently, study of the dayside auroral oval is limited to a short observational window (a few weeks) near winter solstice, from restricted locations (e.g. Svalbard in the northern hemisphere).

Auroral observations by spacecraft have a potentially complete field-of-view of a single hemisphere. Satellite-based imagers, such as Polar UVI [*Torr et al.*, 1995], can image the aurora over an entire polar ionosphere at low spatial resolution (~30 km square at orbit apogee) with better than 1-min temporal resolution for prolonged periods of ~9 hours per 18-hour orbit. A major advantage of spacecraft imagers is the ability to measure UV emissions, which cannot be detected at the ground due to atmospheric absorption.

UV imagers have the advantage of being able to make observations in sunlight, although dayglow can dominate over the auroral emission at times.

An understanding of the particle precipitation giving rise to the observed auroral luminosity allows the probable source regions, and hence the boundaries between regions, to be identified. The more energetic (harder) particles typical of the outer magnetosphere penetrate more deeply into the atmosphere before dissipating their energy than the less energetic (softer) particles found, for example, in the magnetosheath [e.g., *Rees*, 1963]. In the dayside ionosphere the OCB is often identified on the ground as the poleward edge of luminosity dominated by green-line emissions (557.7 nm - characteristic of the E-region) resulting from harder precipitation in the magnetosphere and the equatorward edge of red-line dominated luminosity (630.0 nm - characteristic of the F-region) resulting from softer magnetosheath precipitation [*Lockwood et al.*, 1993]. The ratio of the luminosity of the red- and green-lines at a certain location gives an indication of the characteristic energy of the precipitating particles. In the nightside ionosphere, both the red- and green-line emissions correspond to precipitation on closed field lines and the open field line region is typically void of auroral emissions. Thus the OCB is identified as the poleward boundary of either of these emissions, although the red line is thought to be the best indicator [*Blanchard et al.*, 1995].

Space-based observations have been made in a range of UV wavelength bands. Although the auroral oval is typically clearly displayed at most UV wavelengths, it is not a trivial task to determine the OCB from these images. It is uncertain whether the OCB corresponds best to an absolute auroral intensity threshold or to a fraction of a maximum intensity. There have been few inter-instrument comparisons which have addressed this uncertainty. However, a comprehensive comparison of Polar UVI and DMSP particle precipitation boundaries by *Carbary et al.* [2003], using images in the Lyman-Birge-Hopfield long (LBHL) auroral emission band (∼160-180 nm), showed that the poleward edge of the auroral oval in the dayside ionosphere was co-located with the OCB. (The intensity in the LBHL band is considered to be proportional to the energy flux of precipitating electrons [*Germany et al.*, 1997].) The method of *Carbary et al.* [2003] fits a Gaussian plus a background quadratic function to a latitudinal profile of the UVI-LBHL auroral image intensity in a 1-hr MLT bin, and then locates the boundary estimate at a fixed point on this function (at a distance equivalent to the full-width-at-half-maximum of the Gaussian poleward of the Gaussian peak). The LBHL boundary also matches well to the OCB for much of the nightside ionosphere, although an offset (∼3°) exists in the early morning sector [*Kauristie et al.*, 1999; *Baker et al.*, 2000; *Carbary et al.*, 2003]. In this sector, the poleward boundary of shorter wavelength UV emissions in the 130-140 nm range appears to provide a more reliable proxy for the OCB [*Wild et al.*, 2004]. During active geomagnetic conditions, such as the substorm expansion phase, the nightside boundary is relatively clear, as the substorm auroral bulge is a well-defined feature that can be readily identified in auroral imagery. During more quiescent times, however, the nightside oval can become relatively faint, such that it is difficult to identify the poleward edge of the oval with any great certainty. At these times, the accuracy of the OCB determination will depend on the sensitivity of the auroral imager.

For our example event study we use the OCB proxy identified in auroral images measured by Polar UVI in the LBHL emission range. Suitable ground-based auroral observations were not available for this interval. In fig.6 we show the auroral image measured by Polar UVI-LBHL at 2017:34 UT on 26 December 2000 (overlapping the time interval of the convection map shown in fig.5). The orbital position of the polar spacecraft means that the image coverage is restricted predominantly to the nightside auroral oval. The viewing angle of the spacecraft at this time is such that the resolution in the morning sector is poorer, and hence more uncertainties will be introduced here. The auroral oval is clearly visible, being characterised by the higher intensity emissions. The UVI proxy for the OCB is determined by averaging the image intensities measured in 1° latitude by 1-hr MLT sectors and then using the method of *Carbary et al.* [2003], fitting a function to the latitudinal intensity profiles, as discussed above.

Figure 7 presents examples of these fits from the 0100-0200, 1800-1900, and 2300-2400 MLT sectors (those regions marked with the blue radial lines in fig.6). The top two panels illustrate locations where the fit (dotted line) to the auroral intensity profile (solid histogram) is very good, although in one case the auroral region covers a much larger latitudinal range than the other. The boundaries determined in these cases (dashed vertical line) appear reasonable and would match closely with other boundary determination methods. In the final panel the intensity variation appears double-peaked and so the fit is not so good (although the fit does pass the quality controls set by *Carbary et al.* [2003]). As a result, the boundary is placed at a slightly higher latitude than may result from other techniques. This highlights that this technique has a weakness when the latitudinal intensity profile is characterised by more than one peak. A more sophisticated technique which is suitable for fitting more than one peak may be an improvement on this method. Notwithstanding this potential weakness in this technique, we still use this method of boundary determination in this paper as it is the only one which has been calibrated with an independent OCB data set.

The boundaries determined in this way are shown as black symbols in fig.6. We further use the statistical boundary offsets determined by *Carbary et al.* [2003] to adjust our measured boundaries to provide more accurate estimates of the OCB. (This is especially significant for the measurements in the early morning sector ionosphere). The adjusted boundaries are shown as red symbols in fig.6. Hence, the UVI observations at this time provide us with OCB estimates across much of the nightside ionosphere. However, they provide no information about the OCB in the 0700–1700 MLT range.

2.3.3. The Doppler spectral width boundary

The Doppler spectral width of backscatter measured by the SuperDARN HF radar network is a parameter that reflects the spatial and temporal structure of ionospheric electron density irregularities convecting in the ionospheric convection electric field [*André et al.*, 2000]. As with precipitating particles and auroral observations, the spectral width varies between regions of different magnetic connectivity and hence across the reconnection separatrix/OCB, although the physical reasons for these variations are not yet fully understood [*Ponomarenko and Waters*, 2003]. *Baker et al.* [1995] first showed that regions of enhanced Doppler spectral width were associated with regions of cusp particle precipitation and that the spectral width was reduced equatorward of the cusp. The transition between these low and high spectral width regions has been termed the spectral width boundary (SWB) and has subsequently been shown to be a typical feature at all MLTs and not just in the cusp regions [*Chisham and Freeman*, 2004]. If the SWB was co-located with the OCB at all MLTs then the extensive spatial and temporal coverage of the SuperDARN radars would allow for the possibility of prolonged monitoring of the separatrix location and motion. However, methods of detection of the SWB and a full understanding of how the boundary relates to the OCB have a history of confusion with conflicting conclusions drawn in different studies.

Threshold techniques have been employed to objectively identify the SWB in cusp-region SuperDARN backscatter for some years [*Baker et al.*, 1997; *Chisham et al.*, 2001]. These techniques involve choosing a spectral width threshold value above which the spectral width values are more likely to originate from the distribution of spectral width values typically found poleward of the OCB, and developing an algorithm that searches poleward along a radar beam until this threshold is exceeded. *Chisham and Freeman* [2003] showed that this technique can be inaccurate in its simplest form as the probability distributions of the spectral width values poleward and equatorward of the SWB are typically broad and have considerable overlap. They showed that the inclusion of additional rules in the threshold algorithm, such as spatially and temporally median filtering the spectral width data, increased the accuracy of the estimation of the SWB location. They termed their method the 'C-F threshold technique', and that is what we use for our example event analysis in this paper. *Chisham and Freeman* [2004] further showed that the technique could be objectively applied to SWBs at all MLTs. However, SWBs rarely approximate infinitely sharp latitudinal transitions in spectral width, and hence, the latitude of the SWB is dependent on the spectral width threshold used [*Chisham and Freeman*, 2004].

To investigate the reliability of the SWBs determined by this method as proxies for the OCB, *Chisham et al.* [2004a, 2005a, c] compared five years of SWBs (determined using spectral width thresholds of 150 and 200 m/s) with the particle precipitation signature of the OCB measured by the DMSP low-altitude spacecraft [*Sotirelis and Newell*, 2000]. These studies showed that the SWB is a good proxy for the OCB at most MLTs, with the exception being in the early morning sector (0200–0800 MLT). (Comparing with the *Carbary et al.* [2003] study, it was found that the SWB is in fact co-located with the poleward edge of the LBHL auroral oval). The SWB is most clearly observed in meridionally-aligned SuperDARN radar beams. As beams become more zonally-aligned, geometrical factors can become major causes of enhanced spectral width and so can place the SWB far equatorward of the OCB location [*Chisham et al.*, 2005b].

For the event being studied in this paper, SWBs were available from a number of the meridionally-aligned SuperDARN radar beams. Importantly, the SWBs measured by the Kapuskasing, Kodiak, and Prince George SuperDARN radars provided estimates of the OCB in the dayside region of the ionosphere not covered by the Polar UVI observations. In fig.8 we illustrate how the C-F threshold technique estimates the SWB for one of these radars at our time of interest (2017 UT on 26 December 2000). Fig.8a presents the raw spectral width values measured by the Kapuskasing radar at this time. Only data from within ±4 beams of the meridional direction are shown and used. The dashed meridional line shows the location of the 1500 MLT meridian. The spectral width values are highly variable and appear to be higher in the western side of the field-of-view than in the eastern. Fig.8b shows the spectral width variation at this time after the data has been spatially and temporally median filtered. The data are spatially filtered across 3 adjacent beams and temporally filtered across 5 adjacent scans, as described by *Chisham and Freeman* [2004]. In fig.8b the longitudinal change in spectral width has become clearer as well as the latitudinal transition from low to high spectral width around 73° which provides our estimate of the OCB.

A threshold method is now applied to the spectral width data in fig.8b to provide our estimates for the OCB location. Fig.8c shows the result of thresholding the spectral width data at 150 m/s (the most suitable spectral width threshold value for this MLT sector). The grey region highlights where the spectral width was less than 150 m/s, the black region where it was greater than 150 m/s. The threshold technique involves searching poleward up each radar beam and finding the first range gate at which the spectral width is greater than 150 m/s and for which two of the subsequent three range gates also have spectral width values greater than 150 m/s. For this time, SWBs could only be determined for the four beams to the western side of the field-of-view. The SWB locations are highlighted by the four white squares in fig.8c. (Note that the absence of a measurable SWB on the eastern side of the field-of-view does not imply the absence of the OCB).

2.3.4. Other proxies

Here, we briefly discuss two further proxies for the OCB that we do not make use of in the event study presented here but which are potentially useful OCB proxies for reconnection rate measurement studies.

The convection reversal boundary (CRB) is located where the ionospheric convection changes from being sunward (typical of closed field lines) to antisunward (typical of open field lines). If all closed field lines flowed sunward and all open field lines flowed antisunward then the CRB and the OCB would coincide. However, there are other factors that influence where one determines the CRB, namely the reference frame of observation(corotating vs. inertial), and the effect of viscous convection cells [*Reiff and Burch*, 1985]. The change in reference frame from inertial to the corotational frame of the SuperDARN observations moves the latitude of the CRB poleward. Considering the contribution from a viscous cell would also move the CRB latitude poleward. *Newell et al.* [1991] showed that the CRB in the inertial frame in the dayside ionosphere was typically located within the LLBL, on closed field lines. *Sotirelis et al.* [2005] performed a large statistical comparison of OCB and CRB locations in the corotation frame at all MLTs and showed that the CRB correlates well with the OCB. They did identify an equatorward offset of the CRB relative to the OCB that varied from zero near noon to $\sim 1°$ near dawn and dusk and to $\sim 2°$ near midnight.

It is also possible to use incoherent scatter radar (ISR) measurements to estimate the OCB location. *Doe et al.* [1997] used ISR to measure the characteristic energies of precipitating electrons across a range of latitudes. Sharp latitudinal gradients in the characteristic energy can be used to estimate the OCB location. Latitudinal transitions in ionospheric electron density measured by ISR can also be used as OCB proxies. Particle precipitation in the auroral oval enhances the electron density in the ionosphere through enhanced ionization. In the nightside ionosphere the poleward boundary of the auroral oval is characterised by a sharp latitudinal cut-off of electron density in the E-region. This density proxy was used in estimating reconnection rates by *de la Beaujardière et al.* [1991] and *Blanchard et al.* [1997].

2.3.5. The effect of convection on offsetting proxies from the true separatrix

In regions where reconnection is ongoing, there is an argument as to how the effects of the convection of newly-reconnected field lines affect the reliability of the ionospheric proxies for the reconnection separatrix. It has been suggested that there typically exists a small (<1°) latitudinal displacement between the true separatrix location and the proxy due to the effects of the convection of newly-reconnected field lines. In the cusp, for example, the fastest precipitating magnetosheath-like ions which characterise the newly-opened field lines take a finite time to travel from the reconnection site (assuming this to be their place of origin) to the ionosphere, during which time the footprints of the field lines down which these ions are traveling have been convected away from the separatrix location [*Rodger and Pinnock*, 1997; *Lockwood*, 1997; *Rodger*, 2000]. Hence, the ionospheric signature of these ions will be observed poleward of the footprint of the field line which presently connects to the reconnection X-line. Here, we assume that any offset due to these effects is smaller than the latitudinal resolution of our velocity vector measurements (∼1° latitude).

2.3.6. Estimating the complete separatrix location and motion from discrete observations

The instrumental techniques described above generally provide discrete measurements of the OCB location at a number of particular times and locations. For small-scale reconnection rate determinations, closely-spaced discrete measurements of the OCB can be employed using the techniques outlined in section 2.1.2. To measure the reconnection rate on a more global scale requires either global OCB measurements or some method of interpolation of sparse measurements of the OCB. The simplest assumption that can be realistically used when interpolating ionospheric OCB estimates is that the OCB can be approximated by a circle (used in calculating reconnection rates by *Pinnock et al.* [2003]). *Holzworth and Meng* [1975] and *Meng et al.* [1977] showed that an off-centre circle in geomagnetic co-ordinates was a good fit to the poleward boundary of quiet auroral arcs and hence, provided a good global estimate of the OCB. However, if the MLT coverage of OCB estimates is relatively extensive then there are better techniques which allow a more accurate characterisation of the boundary.

It is possible to approximate the OCB in terms of a Fourier series of order N_t,

$$\lambda(\mathbf{P}(\phi)) = A_0 + \sum_{n=1}^{N_t} A_n \cos(n\phi + \psi_n) \tag{27}$$

where A_0, A_n and ψ_n are constants of the fit. With sparse measurements of the OCB location a global OCB estimate can be determined by least squares fitting a low order ($N_t < 3$) Fourier series to the measured OCB locations, similar to the approach taken by Holzworth and Meng (1975) for describing the auroral oval. When estimates of the OCB location are available from a wider range of MLTs, higher order Fourier series can be used to better describe the data. However, fitting to such higher order Fourier series is fraught with problems due to the many (2n+1) free parameters, and local minima in the 2n+1 parameter space.

Instead, following the example of *Milan et al.* [2003], we adopt a Fourier series derived from a truncated Fourier transform of the estimated OCB locations. First we divide the polar ionosphere into N_b equally sized MLT bins (the choice of N_b is typically dependent on the spatial and temporal resolution of the available boundary data). For bins where one or more estimates of the OCB exist we take the mean of those estimates as the OCB location at the center of that bin ($\lambda(\mathbf{P}_i), i = 1...N_b$). (This can be a weighted mean if required, e.g., if the estimates from one instrumental source are more reliable than another). For bins where no estimate exists we interpolate between the OCB locations on either side to obtain an estimate of the OCB location for that bin. We then take the Fourier transform of these values and ignore the higher order terms (those greater than

N_t, the order of the Fourier series that we require). This truncated Fourier series can then be used to define the OCB at any MLT. The reason for removing the higher order terms is that a complete Fourier series gives an exact fit to the input estimates and for locations away from the bin centres spurious results may exist (much in the same way as fitting an exact polynomial to data with uncertainties can give rise to unrealistic estimates between data points). It is worth noting that the truncated Fourier series is equivalent to a least squares fit of a Fourier series of this order.

As an example of this process, in fig.9 we illustrate how we detemine the global OCB variation for the interval 2017–2018 UT on 26 December 2000 (the same interval as in previous figures). Often, due to the coarse latitudinal resolution of many techniques used to locate the OCB, the measurement of the OCB latitude contains significant quantization noise which is amplified when determining the time derivative for the boundary motion [*Pinnock et al.*, 1999]. Therefore, it is often advisable to temporally smooth the time series of the boundary location in some way to reduce this effect. Here, we have achieved this by mean filtering across a 3-min interval centred on our minute of interest. The squares in fig.9 show all the UVI boundaries measured for the 3-min interval centred on this time. Similarly, the diamonds show all the SWBs measured for the 3-min interval centred on this time. We take the mean latitude value in each 1-hr MLT sector to determine the global boundary (using $N_b = 24$). This spatiotemporal smoothing provides a level of statistical reliability to the values used in our Fourier expansion, as well as reducing the uncertainty in our individual estimates of the boundary location (we assume this to be by a factor of $\sqrt{N}$, where N is the number of OCB estimates in the bin). In fig.9 we also present the results of characterising the OCB as a truncated Fourier series with $N_t = 6$

(6th order - dashed line) and $N_t = 10$ (10th order - bold solid line), as explained above. Obviously, the wider the extent of the data coverage, the higher the order of the Fourier expansion can be. In this case, where the global coverage is quite good it can be clearly seen that on the nightside, the 10th order expansion fits better to the observed data than does the 6th order. The fits to the data elsewhere are very similar for both orders. Hence we use the 10th order expansion in this study.

It is instructive to study how using different instrumentation, assumptions, and data resolution affects the velocity of the OCB that we ultimately determine and use in the reconnection rate calculations. One way to study this is to look at the distributions of the boundary velocities that we observe in different cases. In fig.10a we show boundary velocity distributions determined from the raw Polar UVI observations for our complete event interval (2000-2200 UT). The solid line shows the distribution of boundary velocities determined using temporally adjacent boundary measurements (every $\sim$37 s). Any effects due to noise/random errors in the determination of the OCB latitude from the UVI data will be clearest in this distribution (i.e., the uncertainties will be largest, equation (24)). The distribution is very broad with significant numbers of velocities with magnitudes of $\sim$4000 m/s or higher (this velocity is equivalent to $\sim 2°$ latitude in a minute). The dashed line shows the distribution of boundary velocities determined using measurements that are 2 samples apart (every $\sim$74 s). It is clear that the width of the distribution has been reduced. Similarly, the dotted line shows the distribution of boundary velocities determined using measurements that are 4 samples apart (every $\sim$148 s). Again, the width of the distribution has been reduced such that there are very few boundary velocities measured greater than $\sim$2000 m/s. This figure shows how data of different temporal resolution, from the same data set, will provide a very different distribution of boundary velocities.

In fig.10b we show boundary velocity distributions determined from the filtered Polar UVI observations for the complete event interval (2000-2200 UT). The solid line shows the distribution of boundary velocities when using the mean-filtered UVI data (3-min averaging window at 1-min resolution). The filtering has the effect of thinning the distribution in a similar way to a reduction in the temporal resolution. This is a result of the reduction of the effects of noise and random errors in the data following this averaging process (as well as the reduction of genuine rapid, large amplitude fluctuations). The dashed and dotted lines in fig.10b present the boundary velocity distributions determined from the 6th and 10th order Fourier series OCBs, respectively. These two distributions are almost identical and hence there is no sign of an enhanced level of fluctuations being introduced for the higher order Fourier series. This further supports our use of the 10th order Fourier expansion in this study.

As discussed in section 2.1.1, the variation in the polar cap area provides information about the net reconnection voltage. Having a global representation of the OCB allows this area to be easily estimated. Assuming a spherical Earth, the polar cap area can be estimated by,

$$A_{pc} = \int_0^{2\pi} (R_E + h)^2 (1 - \sin\lambda(\mathbf{P}(\phi)))\, d\phi \tag{28}$$

In a discrete form, assuming N OCB estimates equally spaced in AACGM longitude ϕ we can write this as,

$$A_{pc} = \frac{2\pi(R_E + h)^2}{N} \sum_{i=0}^{N-1} (1 - \sin\lambda(\mathbf{P}_i)) \tag{29}$$

We can apply these techniques to study the polar cap area for the whole of the two-hour interval being studied on this day (2000–2200 UT) (see following section for complete results).

In fig.11 we present 1-min snapshots of the estimated OCB made every 10 min during this interval. The squares represent the UVI and SWB boundaries used to determine the OCB at each time. The bold lines represent 10th order Fourier expansions at each time. For most of the interval the data coverage is particularly good leading to very reliable global boundary estimates. However, towards the end of the interval the data coverage is more patchy and so the global OCB estimates are less reliable. From fig.11 we can see that initially, the approximately circular polar cap expands, reaching its largest size around ∼2040 UT. At this point the polar cap starts to shrink and becomes more oval shaped around ∼2110 UT. Towards the end of the interval the polar cap shrinks to a small size and the boundary is distinctly non-circular. We quantify this polar cap size variation further in the following section.

3. Reconnection rate measurements

3.1. Spatial variation of the reconnection rate

By combining measurements of the ionospheric convection velocity and of the OCB location and motion at a particular time, we can determine the spatial variation of the reconnection rate at that time using the techniques outlined in section 2.1. In figure 12 we show again the northern hemisphere SuperDARN convection map, originally presented in figure 5, for the 1-min interval that we have focussed on (2017–2018 UT) on 26 December 2000. Overplotted on the convection map is the global OCB location (bold line) as determined for this same interval as shown in fig.9. The next step is to select discrete velocity vectors on, or close to, the OCB which will be used in the reconnection rate estimation. This is a trivial exercise in regions where the vectors are co-located with the OCB. However, there are some regions where the selected vectors are, by necessity, $\sim$0.5°-1.0° away from the OCB. The grey shading in fig.12 highlights the velocity vectors selected for this example interval. Whereas the overlap of vectors with the OCB is good on the dayside (from $\sim$0800 MLT through to 1800 MLT), the coverage on the nightside is not so good with the vectors being sparse from $\sim$2230 to $\sim$0300 MLT and being absent from $\sim$0300 to $\sim$0600 MLT. This is the case for most of the interval under study.

In fig.13 we present the spatial variation (with MLT) of the reconnection rate measurements. Positive reconnection rates relate to flux being added to the polar cap whereas negative reconnection rates relate to flux being removed from the polar cap. Hence for most IMF conditions, including the IMF B_y-dominated conditions observed at this time (see fig.14 for full details of the IMF conditions), we would typically expect positive reconnection rates in the dayside ionosphere and negative reconnection rates in the nightside ionosphere. We present the total estimated reconnection rate for our 1-min interval in fig.13a, but we also separate the measurements into the contributions from the plasma flow ($B_{z_i}|\mathbf{V}_i|\cos\theta_i$ in equation 11) (fig.13b) and the contributions from the boundary motion ($B_{z_i}|\mathbf{V}_{P_i}|\cos\alpha$ in equation 11) (fig.13c). The bold black line and grey shaded region in fig.13a represent the mean and standard deviation of the reconnection rate measurements measured in a 2-hour MLT sliding window. This helps to illustrate the gross features in the spatial variation of the reconnection rate.

The contributions from the plasma flow (panel b) are much as expected for most IMF conditions reflecting the standard two-cell ionospheric convection pattern; poleward flow across the OCB in the dayside ionosphere and equatorward flow across the OCB in the nightside ionosphere. The uncertainties in these measurements are estimated as shown in section 2.1.3. Using the results of *Provan et al.* [2002] as a guide for estimating the uncertainties in 'true' velocity vectors, we estimate the uncertainty in the velocity magnitude as ∼25% ($a_1 = 0.25$) and the uncertainty in the angle the vector makes with the normal to the separatrix as ∼45° ($a_2 = \pi/4 \approx 0.79$). We can then rewrite the error equation (20) as,

$$\varepsilon\langle|\mathbf{V}_i(t)|\cos\theta_i(t)\rangle \approx |\mathbf{V}_i(t)|\left(0.0625\cos^2\theta_i(t) - 0.617\sin^2\theta_i(t)\right)^{\frac{1}{2}}. \qquad (30)$$

and so the uncertainty values range from $0.25|\mathbf{V}_i(t)|$ when $\theta_i(t) = 0°$ to $0.79|\mathbf{V}_i(t)|$ when $\theta_i(t) = 90°$. Hence, the largest uncertainties in the contribution from the plasma flow occur around ∼1500 MLT where the convection flows are aligned close to parallel with the estimated OCB.

The contributions from the boundary motion (fig.13c) are characterised by larger uncertainties. We assume that the latitudinal uncertainty in our raw OCB measurements (from both Polar UVI and SuperDARN SWBs) is ∼0.5° (∼50 km), as discussed in previous sections. As measurements are made every minute, then using equation (24) to provide an estimate of the uncertainty in the separatrix motion would give ∼830 m/s. However, this is reduced by dividing by $\sqrt{N}$ to account for the temporal smoothing over N boundary estimates, as discussed in section 2.3.6. (As an aside, if measurements are made every 5 minutes then the basic uncertainty reduces to ∼165 m/s.) It must also be remembered that there are regions of the boundary (shown by the bold symbols in fig.13c) where gaps in the raw OCB data exist and where the boundary has been interpolated. Hence, the boundary estimates in these regions may be questionable. Figure 13c suggests that the contributions to the total reconnection rate from the boundary motion are as large as those from the plasma flow, but that the magnitude of the contribution is spatially variable.

We can describe the spatial variations in the reconnection rate as shown in figure fig.13a in the following way. In the dayside ionosphere we expect positive reconnection rates which represent magnetic flux being added to the polar cap following reconnection on the dayside magnetopause. This is generally the case in fig.13a although the reconnection rate appears to reduce to zero close to noon. This spatial variation in reconnection rate is consistent with a split reconnection X-line on the magnetopause and matches the variation predicted by the anti-parallel merging hypothesis during conditions dominated by the IMF B_y component close to the winter solstice [*Coleman et al.*, 2001; *Chisham et al.*, 2002], matching the conditions for this example event (see section 3.2). In the nightside ionosphere we expect negative reconnection rates which represent magnetic flux being removed from the polar cap following reconnection in the magnetotail. This is generally the case for most of this interval although there are a couple of regions (∼1830–2000 MLT and ∼0200–0300 MLT) where positive reconnection rates are measured. Most of the contribution towards these positive reconnection rates comes from the boundary motion. As it is unlikely that flux is being added to the polar cap at these locations it is therefore likely that the estimation of the boundary motion is in error and hence, that the uncertainties in the boundary motion have been underestimated in these regions. As discussed in section 2.1.3, measuring reconnection rates at a high temporal resolution (e.g., at the 1-min sampling rate used here) requires a significant accuracy of measurements of the OCB location and motion. The large uncertainties in our results suggest that there are still some improvements to be made before the boundary measurements can be measured accurately enough to fully match the requirements of the 1-min convection measurements.

3.2. Temporal variation of the reconnection potential

Figure 14 presents the temporal variation of the average reconnection rate from both the dayside and nightside ionosphere corresponding to magnetopause and magnetotail reconnection, respectively. To place the reconnection rate measurements in context, panel 14a shows the B_y and B_z components of the IMF for this interval as measured by the ACE spacecraft located upstream in the solar wind. The IMF variations have been shifted by 63 min to account for the solar wind travel time between the spacecraft and the Earth's magnetosphere. Panel 14b shows the associated IMF clock angle. At the start of the interval the IMF is in transition from being predominantly southward (not shown) to being dawnward (at ∼2010 UT). For the rest of the 2-hour interval, although the B_z component is positive, the IMF is very much B_y-dominated with the IMF clock angle fluctuating between -70° and -90°. Although the IMF is slightly northward, the existence of normal two-cell convection at this time (and the previous observations of two-cell convection for these IMF conditions [*Freeman et al.*, 1993; *Ruohoniemi and Greenwald*, 1996]), suggests that reconnection is occurring sunward of the cusp region for these conditions, rather than on the lobe magnetopause. Hence, magnetopause reconnection will be responsible for the addition of flux to the polar cap at the OCB during this interval. The two vertical dashed lines in fig.14 show the timing of a substorm onset and a substorm intensification identified from a combination of auroral brightenings in the Polar UVI data, the occurrence of Pi2 pulsations and the initiation of negative bays in ground-based magnetometer data. These events would be expected to be associated with enhanced reconnection in the magnetotail.

Figure 14c presents the variation in polar cap area during this interval, estimated using the techniques outlined in section 2.3.6. At the start of the interval ($\sim$2000-2040 UT), following the interval of southward IMF, the polar cap is expanding, indicating that magnetic flux is being added to the polar cap by magnetopause reconnection at a faster rate than it is being removed by magnetotail reconnection. Following a substorm onset at $\sim$2037 UT (and hence enhanced magnetotail reconnection) the polar cap starts to contract at $\sim$2040 UT. Following a substorm intensification at $\sim$2051 UT the rate of contraction increases before the polar cap size stabilizes at $\sim$2100 UT. At around $\sim$2120 UT the polar cap appears to start contracting again (although the polar cap areas are less reliable at this time because of the reduction in the global coverage of the OCB estimates). The polar cap reaches a steady, minimum size at $\sim$2130 UT. The measured change in the polar cap area across this interval provides a good estimate of the net reconnection voltage and it is generally clear from the gradient of the curve as to whether magnetopause or magnetotail reconnection is the dominant process at any one time.

If we want to study the temporal variation of the reconnection rate (or voltage) in more detail then we need to be able to differentiate between the magnetopause (dayside) and magnetotail (nightside) reconnection rates. Because we do not always have a full complement of velocity vectors along each of the merging lines it is often difficult to calculate a complete reconnection voltage for either the magnetopause or magnetotail X-line. One alternative, when limited data are available, is to present the average reconnection rate ($< E_{rec} >$) measured along the portions of each merging line over which the measurements were made. If an estimate of the total length of the merging line can also be made then this allows an estimate of the total reconnection voltage along the merging line.

In figs.14d and 14e we present the temporal variations of the average dayside and nightside reconnection rates, respectively (bold black lines). The average dayside (nightside) rates were calculated from vectors sunward (anti-sunward) of the 0600-1800 MLT line. For both the dayside and nightside reconnection rates the level of fluctuation is quite high with the point-to-point variability being of similar size to the average electric field values. However, it is difficult to assess how much of this fluctuation is real, caused by temporal burstiness of the reconnection process, and how much is caused by uncertainties in the measured quantities. The occurrence of 'unphysical' negative reconnection rate measurements in the dayside ionosphere and positive reconnection rate measurements in the nightside ionosphere suggests that there are times when the measurements may be inadequate. This supports our previous suggestion that the OCB cannot presently be measured accurately enough to match the requirements of 1-min convection measurements.

The white lines in figs.14d and 14e present the variation of the average of the average reconnection rates measured within a 15-min sliding window (the grey region represents the average of the error estimates in the same window). The white lines act to highlight the general trends in the reconnection rate variations by removing the point-to-point variability. At the beginning of the interval the average dayside reconnection rate is $\sim$20 mV/m whereas that on the nightside varies between 0 and -10 mV/m. The dayside rate decreases slightly with time to $\sim$10 mV/m, whereas, following the substorm onset, the nightside rate changes to $\sim$-40 mV/m, dominating the dayside rate. At this time, the size of the fluctuations in the nightside rate become much larger, although this may be due to the reduction in the size of the measurable nightside merging line. Towards the end of the interval the average nightside reconnection rate appears to reduce to a similar level as the dayside rate leading to a stability in the polar cap area.

It is possible, using equation (9), to perform a consistency check on the polar cap area and average reconnection rate measurements. Since this requires knowledge of the magnetopause and magnetotail reconnection voltages, we need to assume lengths for the dayside and nightside merging lines. Here, we have derived a large number of polar cap area variations from the average reconnection rate measurements (black lines in figs.14d and e) by assuming merging line lengths from 0.1 hours of MLT to 12.0 hours of MLT (in 0.1 hour steps). Using a least squares fit we have then determined which of these variations best matches the observed polar cap area variation. In fig.15a we present the observed polar cap area variation (as shown in fig.14c). We also show (dashed line) the best fit polar cap area variation determined from the average reconnection rate measurements. The best fit occurred when a dayside merging line length of 12 hours of MLT, and a nightside merging line length of 7.6 hours of MLT, were assumed. Although the general variation of the two curves in fig.15a is very similar, the gradients in the three distinct regions of the curve are slightly different, leading to offsets between the curves at the beginning and end of the data sets.

It is fair to assume that the merging line lengths are unlikely to be constant across the whole of this interval. Consequently, we have split the data set into three distinct sections before repeating the fitting process on each section. The sections were selected by the gradients in the polar cap area variation - where the area is clearly increasing, where the area is sharply decreasing, and where the area is stable or gradually decreasing. Figure 15b presents the best fit polar cap area variations determined from the average reconnection rate measurements in each of these sections. The fits in each section are now very good and follow the measured variations in the polar cap area closely. The merging line lengths which provide the best fits are different in each section. At the beginning of the interval, where the polar cap is expanding and the dayside reconnection rate is dominant over the nightside reconnection rate, the length of the dayside and nightside merging lines are predicted to be 8.0 and 3.2 hours of MLT, respectively. When the polar cap starts to contract at ∼2040 UT not only does the average nightside reconnection rate increase (as shown in fig.14e), but the predicted length of the nightside merging line also increases to 9.2 hours of MLT. The predicted length of the dayside merging line also increases but by a smaller amount to 10.0 hours of MLT. When the speed of contraction of the polar cap reduces at ∼2105 UT the predicted length of the nightside merging line reduces slightly to 7.2 hours of MLT, whereas that of the dayside merging line increases slightly to 12.0 hours of MLT.

4. Discussion and Conclusions

So far in this paper we have provided a synthesis of the techniques for measuring the ionospheric projection of the magnetic reconnection rate (section 2) and given an example of its application (section 3). The final stage of ionospheric remote sensing of reconnection is mapping of the measurements in the ionosphere to the reconnection site on the magnetopause or magnetotail. This mapping is essential for a full understanding of the reconnection process because it is at these locations that reconnection actually takes place. However, in our view, it is not yet clear how best to do this mapping and it is also probably subject to large systematic and random uncertainty. For this reason, we have not included mapping in the main technique section but instead discuss here the two main options and their associated problems and uncertainties.

Ideally, one would like to perform an inverse mapping of ionospheric measurements of the reconnection electric field to the reconnection site to provide an estimate of the in-situ reconnection rate [*Pinnock et al.*, 2003; *Chisham et al.*, 2004b]. This may be achieved using a magnetospheric magnetic field model under the assumption that the electric potential is invariant along a magnetic field line. At present, the state of the art in magnetosphere models is the Tsyganenko model [*Tsyganenko*, 1995; *Tsyganenko and Stern*, 1996], the most widely used model in this context. The major difficulty with a magnetic field model such as the Tsyganenko model is that it is derived in part from large sets of spacecraft data, and represents the average configuration of the magnetospheric field, given a particular set of input parameters. The magnetic field at a particular instant may deviate from this configuration, rendering the field line tracing inaccurate. Furthermore, any error in the initial position in the ionosphere is amplified under inverse mapping due to the general divergence of the magnetic field with altitude. Inverse mapping is most reliable in the steady state (when variations in the magnetospheric field are small) and in the dayside ionosphere (where the model fields are typically more reliable), such as in the remote sensing studies of *Pinnock et al.* [2003] and *Chisham et al.* [2004b]. However, inverse mapping has not been applied to the remote sensing of magnetotail reconnection during a substorm, such as the case study presented in this paper and that presented by *Lam et al.* [2006], because the magnetic field model of the magnetotail will be unreliable at times of rapidly changing magnetic field (e.g., at substorm onset). The accuracy of, and confidence in, inverse mapping can be improved by calibrating with in-situ spacecraft measurements where available. For example, *Pinnock et al.* [2003] used magnetopause crossings identified by the Geotail and Equator-S satellites to re-scale the size of the Tsyganenko model used in their mapping (by adjusting the solar wind dynamic pressure input) and showed that the remotely sensed reconnection rate was consistent with in-situ point samples in location and magnitude. The importance of accurate inverse mapping to the interpretation of observations is well illustrated in the results of *Chisham et al.* [2002] where the reconnection electric field in the ionosphere is highly asymmetric (being high in the post-noon sector, and low in the pre-noon sector) but is relatively symmetric when mapped to the magnetopause [*Freeman et al.*, 2007].

Currently, the more reliable way of using the ionospheric remote sensing technique to study reconnection problems is to use a forward mapping method. In this approach a reconnection model or scenario is tested by predicting the ionospheric projection of the reconnection electric field for direct comparison with the remote sensing observations. This has the advantage over inverse mapping in that positional uncertainties at the reconnection site decrease on mapping to the ionosphere rather than grow. In addition, the effects of instrument error, data gaps, and data assimilation methods can be more readily simulated. Even better is to use forward mapping to test alternative reconnection models within a common global framework. In this case the different reconnection models are both subject to similar errors from the magnetic field model and other effects in the forward mapping. Hence, the acceptance of a reconnection model is based on relative, rather than absolute, agreement with the observations. This was effectively the approach used by *Coleman et al.* [2001] and *Chisham et al.* [2002] to differentiate between the subsolar and anti-parallel models of reconnection. In these studies a distinctive difference in the variation of the electric field along the ionospheric projection of the magnetopause X-line was identified between the two reconnection models for specific IMF, magnetic dipole tilt, and polar hemisphere conditions that, when compared to observations, provided evidence in favour of the anti-parallel reconnection model.

Whether using inverse or forward mapping, ionospheric remote sensing of reconnection relies on a connection between the reconnection site and the ionosphere by a magnetic field line. If multiple reconnection X-lines exist simultaneously, this can mean that some of these sites are effectively invisible to the ground. For example, during the substorm expansion phase, near-Earth and distant magnetotail reconnection sites are expected to co-exist. Assuming dawn-dusk symmetry, near-Earth reconnection initially reconnects closed magnetic flux created by the distant reconnection site and both sites are connected to the ionosphere, but at a later time near-Earth reconnection reconnects open magnetic flux and detaches the distant reconnection site from the ionosphere. In the case of self-organised criticality or turbulent reconnection, numerous reconnection sites are expected to co-exist [*Klimas et al.*, 2000] and it is unlikely that all of these will connect to the ionosphere. Thus an inverse mapping of the ionospheric reconnection electric field will not give a valid representation of the reconnection scenario, but it may be possible to predict the structure of the ionospheric projection of the reconnection electric field using forward mapping, to compare with observation.

Assuming that a connection between the reconnection X-line and the ionosphere exists, it is crucial to be able to identify the ground-based projection of the reconnection X-line. As discussed in section 2.3, doing this usually involves exploiting the differences in the particle precipitation signatures between open and closed magnetic field lines.

However, when reconnection only reconfigures magnetic field lines, and does not change the magnetic topology (such as with lobe reconnection during northward IMF conditions), then other identifiers are required. For northward IMF conditions, a suitable identifier can be the velocity dispersion of precipitating ions from the reconnection site. Similar velocity-dispersed ion signatures are also seen in the nightside auroral zone and could be an identifier for near-earth reconnection during the early substorm expansion phase.

In conclusion, we have provided a synthesis of the technique for remotely sensing the magnetic reconnection rate from the ionosphere and discussed associated problems and uncertainties. In doing so, we have shown how the remote sensing technique has developed from single point measurements to covering a wide range of spatial scales almost up to the global scale. The example event presented here demonstrates that remote sensing of an entire reconnection X-line is viable by a combination of the existing SuperDARN network and spacecraft auroral imagers, which would be unfeasible by in-situ spacecraft. Further expansion of SuperDARN in both the northern and southern hemispheres is planned [*Chisham et al.*, 2007]. This coincides with an era of unprecedented auroral imaging with the forthcoming NASA Themis mission and its associated ground-based instruments, and future missions such as the Chinese (and European) Space Agency Kuafu spacecraft. These will give continuous observations of the auroral oval in one hemisphere and regular observations of the auroral oval in both hemispheres. This expansion in instrumentation should allow remote sensing of both magnetopause and magnetotail reconnection sites completely and simultaneously.

This remote sensing capability opens up new opportunities for understanding the reconnection process that is fundamental to the behaviour of not only the Earth's magnetosphere but to many natural astrophysical environments and artificial fusion reactors. Progress has already been made in using the remote sensing technique to address the outstanding reconnection questions of the Earth's environment posed in the Introduction, concerning the location, extent and controlling factors of reconnection: The reconnection X-line at the magnetopause has been found to extend over 38 R_E under stable due southward IMF conditions, corresponding to the entire dayside equatorial magnetopause and beyond the dawn and dusk flanks into the magnetotail [*Pinnock et al.*, 2003]. In contrast, for stable due northward IMF the reconnection X-line was found to be limited to 6-11 R_E in the high-latitude lobes of the magnetotail [*Chisham et al.*, 2004b]. For intermediate IMF orientations, the remote sensing technique has provided evidence that the reconnection X-line at the magnetopause is bifurcated, existing in two distinct regions on the high latitude magnetopause equatorward of the cusps [*Coleman et al.*, 2001; *Chisham et al.*, 2002]. This is in contrast to the single magnetopause X-line extending between these regions through the subsolar region that is inferred for these IMF conditions from in-situ spacecraft observations [*Fear et al.*, 2005]. This paradox needs to be reconciled. In the magnetotail, the ionospheric projection of the reconnection X-line is found to increase in length following substorm onset, in one case from 3.2 hours of MLT in the substorm growth phase to 9.2 hours of MLT in the substorm expansion phase (see example discussed in previous section) and in another from 4 hours to 7 hours of MLT in the first 15 min of the expansion phase [*Lam et al.*, 2006], although the corresponding location and length of the reconnection X-line in the magnetotail has not been estimated in these cases (as discussed above).

The reconnection questions being addressed in the terrestrial context have relevance to more general reconnection problems. For example, the remote sensing measurements of magnetopause reconnection summarised above argue that reconnection is restricted to regions of high magnetic shear and that consequently the relative geometry of magnetic fields is the principal factor determining the overall reconnection rate [*Freeman et al.*, 2007], and hence, the dynamical behaviour of magnetised plasmas in general, an assumption that is invoked in the context of the solar corona [*Hughes et al.*, 2003]. With the development of the remote sensing technique and the existing and forthcoming data from SuperDARN and auroral imagers, measurement of reconnection could become increasingly efficient and routine. This should allow us to address more conclusively the particularly important problem of the general structure of reconnection in time and space, including its temporal continuity and stability [*Phan et al.*, 2000; *Abel and Freeman*, 2002], and the relative prevalence and causes of single, dual, or multiple reconnection sites with particular scales, or of scale-free reconnection structure [*Lazarian and Vishniac*, 1999; *Klimas et al.*, 2000; *Coleman et al.*, 2001; *Chisham et al.*, 2002; *Coleman and Freeman*, 2005; *Phan et al.*, 2006].

Glossary

Altitude-adjusted corrected geomagnetic (AACGM): A geomagnetic coordinate system defined to be the same as the corrected geomagnetic coordinate (CGM) system at 0 km altitude. At all other altitudes the system is defined so that latitude and longitude are invariant along a magnetic field line.

Aurora: Natural coloured-light displays in the polar regions caused by the collision of charged particles from the Earth's magnetosphere with atoms in the upper atmosphere.

Closed field line: A geomagnetic field line that has both ends connected to the Earth.

Coherent scatter radar: Coherent scatter radar is a volume scattering technique where the radar detects energy scattered from within a medium when there are regular spatial variations of the refractive index due to density irregularities. This is the analogue of Bragg scattering of X-rays from crystals. The term "coherent" applies to the constructive interference possible when there is a scattering structure with an organized spatial content at half the radar wavelength.

Convection reversal boundary (CRB): This is located where ionospheric convection changes from being sunward to antisunward.

Cross-polar cap potential: The electric potential difference measured from dawn to dusk across the polar cap.

Cusp: A region of the dayside magnetosphere in which the entry of magnetosheath plasma to low altitudes is most direct.

Defense meteorological satellite program (DMSP): A series of low-altitude spacecraft which monitor meteorological, oceanographic, and solar-terrestrial physics for the United States Department of Defense.

Doppler spectral width: The width of Doppler spectra of ionospheric density irregularities measured by the SuperDARN radars.

E-region: A layer of the ionosphere that exists at about 90-150 km altitude.

F-region: A layer of the ionosphere that exists at about 150-800 km altitude.

Flux transfer events (FTE): Bursty and/or patchy reconnection events that occur on the dayside magnetopause.

Incoherent scatter radar: Incoherent scatter radar is a technique where radio signals are scattered from a large number of individual electrons in random thermal motion in the ionosphere. The technique allows measurements of the density, temperature, velocity, and composition of ionospheric ions and electrons.

Interplanetary magnetic field (IMF): The Sun's magnetic field carried by the solar wind through the solar system.

Ionosphere: The ionized region of the upper atmosphere, forming the lower boundary of the magnetosphere.

Ionospheric irregularities: Density structures in the E- and F-region ionosphere which act as backscatter targets for coherent scatter radar signals.

Lobes: Regions of low density plasma in the Earth's magnetotail. They are constituted of open geomagnetic field lines which originate in both polar ionospheres.

Magnetic local time (MLT): A measurement of local time (i.e., a position relative to the Earth-Sun direction) in the AACGM coordinate system.

Magnetic reconnection: A process which changes the connectivity and topology of magnetic field line regions and facilitates the transfer of mass, momentum and energy between these regions.

Magnetopause: The outer limit of the magnetosphere where the magnetic pressure of the magnetosphere is balanced by the kinetic pressure of the solar wind.

Magnetosphere: The region of near-Earth space where the geomagnetic field has dominant control over the motion of plasma.

Magnetotail: That part of the magnetosphere that is stretched out anti-sunward of the Earth by the solar wind.

Merging line: The ionospheric projection of the reconnection separatrix.

Near-Earth neutral line (NENL): A neutral line (X-line) that is thought to occur earthward of the magnetotail X-line around the time of substorm onset.

Neutral point: The point at the centre of a region of magnetic reconnection where the field strength is effectively zero.

Open field line: A geomagnetic field line that has only one end connected to the Earth, and which also forms part of the interplanetary magnetic field.

Open-closed field line boundary (OCB): The boundary between open and closed geomagnetic field lines which is equivalent to the reconnection separatrix for most IMF conditions.

Plasma: An ionized gas composed of electrons and ions.

Polar cap: The ionospheric footprint of the region of open geomagnetic field lines. Polar caps exist in both the northern and southern hemisphere ionospheres.

Polar cap boundary: The ionospheric footprint of the open-closed field line boundary.

Polar ultra-violet imager (UVI): An instrument on the NASA Polar satellite which takes global-scale images of the aurora at ultra-violet wavelengths.

Reconnection rate: The reconnection rate (or reconnection electric field) is defined as the rate of transfer of magnetic flux across unit length of the reconnection separatrix. The units of reconnection rate are V/m or Wb/s/m.

Reconnection separatrix: Separatrix surfaces divide different magnetized plasma domains. The reconnection separatrix is the boundary between unreconnected and reconnected magnetic field lines.

Reconnection voltage: The reconnection voltage (or integrated reconnection rate) is the magnetic flux transfer associated with an extended X-line. The units of reconnection voltage are V or Wb/s.

Solar wind: A stream of plasma, ejected from the upper atmosphere of the Sun, which flows radially outward through interplanetary space.

Space weather: Space weather describes the conditions in space that affect the Earth and its technological systems, and is affected by factors such as the behavior of the Sun and the nature of the Earth's magnetic field.

Spectral width boundary (SWB): The boundary between ionospheric backscatter spectra with high and low spectral widths as measured by the SuperDARN HF radar network. This boundary is often a good proxy for the open-closed field line boundary.

Substorm cycle: The slow build-up and rapid release of magnetic energy within the Earth's magnetosphere.

SuperDARN: The Super Dual Auroral Radar Network - an international radar network for studying the upper atmosphere and ionosphere, comprised of twelve radars in the northern hemisphere and seven in the southern hemisphere that operate in the High Frequency (HF) bands between 8 and 22 MHz. The radars measure the Doppler velocity of plasma density irregularities in the ionosphere.

SuperDARN global convection mapping: This technique (also known as Map Potential) fits line-of-sight velocity data from multiple SuperDARN radars to an expansion of the ionospheric electric potential in spherical harmonics to produce global ionospheric convection maps.

Tsyganenko model: The Tsyganenko model is a semi-empirical best-fit representation for the Earth's magnetic field, based on a large number of near-Earth satellite observations.

X-line: An extended line of X-type neutral points along the reconnection separatrix.

Acknowledgments. We are grateful to all the national funding agencies for continued support for the SuperDARN radar network. We thank George Parks (Space Sci. Lab., Berkeley) for providing Polar UVI data.

References

Abel, G. A., and Freeman, M. P. (2002), A statistical analysis of ionospheric velocity and magnetic field power spectra at the time of pulsed ionospheric flows, *J. Geophys. Res.*, *107*, 1470, doi:10.1029/2002JA009402.

André, R., Pinnock, M., Villain, J.-P., and Hanuise, C. (2000), On the factors conditioning the Doppler spectral width determined from SuperDARN HF radars, *Int. J. Geomagn. Aeron.*, *2*, 77–86.

Axford, W. I., and Hines, C. O. (1961), A unifying theory of high-latitude geophysical phenomena and geomagnetic storms, *Can. J. Phys.*, *39*, 1433–1464.

Baker, K. B., and Wing, S. (1989), A new magnetic coordinate system for conjugate studies at high latitudes, *J. Geophys. Res.*, *94*, 9139–9143.

Baker, K. B., Dudeney, J. R., Greenwald, R. A., Pinnock, M., Newell, P. T., Rodger, A. S., Mattin, N., and Meng, C.-I. (1995), HF radar signatures of the cusp and low-latitude boundary layer, *J. Geophys. Res.*, *100*, 7671–7695.

Baker, K. B., Rodger, A. S., and Lu, G. (1997), HF-radar observations of the dayside magnetic merging rate: A Geospace Environment Modeling boundary layer campaign study, *J. Geophys. Res.*, *102*, 9603–9617.

Baker, J. B., Clauer, C. R., Ridley, A. J., Papitashvili, V. O., Brittnacher, M. J., and Newell, P. T. (2000), The nightside poleward boundary of the auroral oval as seen by DMSP and the Ultraviolet Imager, *J. Geophys. Res.*, *105*, 21267–21280.

Blanchard, G. T., Lyons, L. R., Samson, J. C., and Rich, F. J. (1995), Locating the polar cap boundary from observations of 6300 Å emission, *J. Geophys. Res.*, *100*, 7855–7862.

Blanchard, G. T., Lyons, L. R, de la Beaujardière, O., Doe, R. A., and Mendillo, M. (1996), Measurement of the magnetotail reconnection rate, *J. Geophys. Res.*, *101*, 15,265–15,276.

Blanchard, G. T., Lyons, L. R, and de la Beaujardière, O. (1997), Magnetotail reconnection rate during magnetospheric substorms, *J. Geophys. Res.*, *102*, 24,303–24,312.

Blanchard, G. T., Ellington, C. L., Lyons, L. R., and Rich, F. J. (2001), Incoherent scatter radar identification of the dayside magnetic separatrix and measurement of magnetic reconnection, *J. Geophys. Res.*, *106*, 8185–8195.

Burch, J. L., Reiff, P. H., Spiro, R. W., Heelis, R. A., and Fields, S. A. (1980), Cusp region particle precipitation and ion convection for northward interplanetary magnetic field, *Geophys. Res. Lett.*, *7*, 393–396.

Carbary, J. F., Sotirelis, T., Newell, P. T., and Meng, C.-I. (2003), Auroral boundary correlations between UVI and DMSP, *J. Geophys. Res.*, *108*, 1018, doi:10.1029/2002JA009378.

Chisham, G., Pinnock, M., and Rodger, A. S. (2001), The response of the HF radar spectral width boundary to a switch in the IMF B_y direction: Ionospheric consequences of transient dayside reconnection? *J. Geophys. Res.*, *106*, 191–202.

Chisham, G., and Pinnock, M. (2002), Assessing the contamination of SuperDARN global convection maps by non-F-region backscatter, *Ann. Geophys.*, *20*, 13–28.

Chisham, G., Coleman, I. J., Freeman, M. P., Pinnock, M., and Lester, M. (2002), Ionospheric signatures of split reconnection X-lines during conditions of IMF $B_z < 0$ and $|B_y| \sim |B_z|$: Evidence for the anti-parallel merging hypothesis, *J. Geophys. Res.*, *107*(A10), 1323, doi:10.1029/2001JA009124.

Chisham, G., and Freeman, M. P. (2003), A technique for accurately determining the cusp-region polar cap boundary using SuperDARN HF radar measurements, *Ann. Geophys.*, *21*, 983–996.

Chisham, G., and Freeman, M. P. (2004), An investigation of latitudinal transitions in the SuperDARN Doppler spectral width parameter at different magnetic local times, *Ann. Geophys.*, *22*, 1187–1202.

Chisham, G., Freeman, M. P., and Sotirelis, T. (2004a), A statistical comparison of SuperDARN spectral width boundaries and DMSP particle precipitation boundaries in the nightside ionosphere, *Geophys. Res. Lett.*, *31*, L02804, doi:10.1029/2003GL019074.

Chisham, G., Freeman, M. P., Coleman, I. J., Pinnock, M., Hairston, M. R., Lester, M., and Sofko, G. (2004b), Measuring the dayside reconnection rate during an interval of due northward interplanetary magnetic field, *Ann. Geophys.*, *22*, 4243–4258.

Chisham, G., Freeman, M. P., Sotirelis, T., Greenwald, R. A., Lester, M., and Villain, J.-P. (2005a), A statistical comparison of SuperDARN spectral width boundaries and DMSP particle precipitation boundaries in the morning sector ionosphere, *Ann. Geophys.*, *23*, 733–743.

Chisham, G., Freeman, M. P., Sotirelis, T., and Greenwald, R. A. (2005b), The accuracy of using the spectral width boundary measured in off-meridional SuperDARN HF radar beams as a proxy for the open-closed field line boundary, *Ann. Geophys.*, *23*, 2599–2604.

Chisham, G., Freeman, M. P., Lam, M. M., Abel, G. A., Sotirelis, T., Greenwald, R. A., and Lester, M. (2005c), A statistical comparison of SuperDARN spectral width boundaries and DMSP particle precipitation boundaries in the afternoon sector ionosphere, *Ann. Geophys.*, *23*, 3645–3654.

Chisham, G., Lester, M., Milan, S. E., Freeman, M. P., Bristow, W. A., Grocott, A., McWilliams, K. A., Ruohoniemi, J. M., Yeoman, T. K., Dyson, P. L., Greenwald, R. A., Kikuchi, T., Pinnock, M., Rash, J. P. S., Sato, N., Sofko, G. J., Villain, J.-P., and Walker, A. D. M. (2007), A decade of the Super Dual Auroral Radar Network (SuperDARN): Scientific achievements, new techniques and future directions, *Surv. Geophys.*, *28*, 33–109.

Coleman, I. J., Chisham, G., Pinnock, M., and Freeman, M. P. (2001), An ionospheric convection signature of antiparallel reconnection, *J. Geophys. Res.*, *106*, 28995–29007.

Coleman, I. J., and Freeman, M. P. (2005), Fractal reconnection structures on the magnetopause, *Geophys. Res. Lett.*, *32*, L03115, doi:10.1029/2004GL021779.

Cowley, S. W. H. (1981), Magnetospheric asymmetries associated with the Y component of the IMF, *Planet. Space Sci.*, *28*, 79–96.

Cowley, S. W. H., and Lockwood, M. (1992), Excitation and decay of solar wind-driven flows in the magnetosphere-ionosphere system, *Ann. Geophys.*, *10*, 103–115.

de la Beaujardière, O., Lyons, L. R., and Friis-Christensen, E. (1991), Sondrestrom radar measurements of the reconnection electric field, *J. Geophys. Res.*, *96*, 13907–13912.

Doe, R. A., Vickrey, J. F., Weber, E, J., Gallagher, H. A., and Mende, S. B. (1997), Ground-based signatures for the nightside polar cap boundary, *J. Geophys. Res.*, *102*, 19989–20005.

Dungey, J. W. (1961), Interplanetary field and auroral zones, *Phys. Rev. Lett.*, *6*, 47-48.

Dungey, J. W. (1963), The structure of the ionosphere, or adventures in velocity space, in *Geophysics: The Earth's Environment*, edited by C. DeWitt, J. Hiebolt, and A. Lebeau, pp. 526–536, Gordon and Breach, New York.

Fear, R. C., Fazakerley, A. N., Owen, C. J., and Lucek, E. A. (2005), A survey of flux transfer events observed by Cluster during strongly northward IMF, *Geophys. Res. Lett.*, *32*, L18105, doi:10.1029/2005GL023811.

Freeman, M. P., Farrugia, C. J., Burlaga, L. F., Hairston, M. R., Greenspan, M. E., Ruohoniemi, J. M., and Lepping, R. P. (1993), The interaction of a magnetic cloud with the Earth: Ionospheric convection in the northern and southern hemispheres for a wide range of quasi-steady interplanetary magnetic field conditions, *J. Geophys. Res.*, *98*, 7633–7655.

Freeman, M. P., Chisham, G., and Coleman, I. J. (2007), Remote sensing of reconnection, chapter 4.6, in Reconnection of Magnetic Fields, edited by Joachim Birn and Eric Priest, Cambridge University Press.

Germany, G. A., Parks, G. K., Brittnacher, M., Cumnock, J., Lummerzheim, D., Spann, J. F., Chen, L., Richards, P. G., and Rich, F. J. (1997), Remote determination of auroral energy characteristics during substorm activity, *Geophys. Res. Lett.*, *24*, 995–998.

Greenwald, R. A., Baker, K. B., Dudeney, J. R., Pinnock, M., Jones, T. B., Thomas, E. C., Villain, J.-P., Cerisier, J.-C., Senior, C., Hanuise, C., Hunsucker, R. D., Sofko, G., Koehler, J., Nielsen, E., Pellinen, R., Walker, A. D. M., Sato, N., and Yamagishi, H. (1995), DARN/SuperDARN: A global view of the dynamics of high-latitude convection, *Space Sci. Rev.*, *71*, 761–796.

Hill, T. W., and Reiff, P. H. (1977), Evidence of magnetospheric cusp proton acceleration by magnetic merging at the dayside magnetopause, *J. Geophys. Res.*, *82*, 3623–3628.

Holzworth, R. H., and Meng, C.-I. (1975), Mathematical representation of the auroral oval, *Geophys. Res. Lett.*, *2*, 377–380.

Huang, C.-S., Sofko, G. J., Koustov, A. V., André, D. A., Ruohoniemi, J. M., Greenwald, R. A., and Hairston, M. R. (2000), Evolution of ionospheric multicell convection during northward interplanetary magnetic field with $|B_z/B_y| > 1$, *J. Geophys. Res.*, *105*, 27095–27108.

Hubert, B., Milan, S. E., Grocott, A., Blockx, C., Cowley, S. W. H., and Gérard, J.-C. (2006), Dayside and nightside reconnection rates inferred from IMAGE-FUV and Super Dual Auroral Radar Network data, *J. Geophys. Res.*, *111*, A03217, doi:10.1029/2005JA011140.

Hughes, D., Paczuski, M., Dendy, R. O., Helander, P., and McClements, K. G. (2003), Solar flares as cascades of reconnecting magnetic loops, *Phys. Rev. Lett.*, *90*, 131101.

Imber, S. M., Milan, S. E., and Hubert, B. (2006), The auroral and ionospheric flow signatures of dual lobe reconnection, *Ann. Geophys.*, *24*, 3115–3129.

Kauristie, K., Weygand, J., Pulkkinen, T. I., Murphree, J. S., and Newell, P. T. (1999), Size of the auroral oval: UV ovals and precipitation boundaries compared, *J. Geophys. Res.*, *104*, 2321–2331.

Klimas, A. J., Valdivia, J. A., Vassiliadis, D., Baker, D. N., Hesse, M., and Takalo, J. (2000), Self-organized criticality in the substorm phenomenon and its relation to localized reconnection in the magnetospheric plasma sheet, *J. Geophys. Res.*, *105*, 18765–18780.

Lam, M. M., Pinnock, M., and Donovan, E. F. (2006), Observations of nightside magnetic reconnection during substorm growth and expansion phases, *J. Geophys. Res.*, *111*, A05209, doi:10.1029/2005JA011356.

Lazarian, A., and Vishniac, E. T. (1999), Reconnection in a weakly stochastic field, *Astrophys. J.*, *517*, 700–718.

Lewis, R. V., Freeman, M. P., and Reeves, G. D. (1998), The relationship of HF radar backscatter to the accumulation of open magnetic flux prior to substorm onset, *J. Geophys. Res.*, *103*, 26613–26619.

Lindqvist, P.-A., and Mozer, F. S. (1990), The average tangential electric field at the noon magnetopause, *J. Geophys. Res.*, *95*, 17137–17144.

Lockwood, M. (1997), Relationship of dayside auroral precipitations to the open-closed separatrix and the pattern of convective flow, *J. Geophys. Res.*, *102*, 17475–17487.

Lockwood, M., and Smith, M. F. (1992), The variation of reconnection rate at the dayside magnetopause and cusp ion precipitation, *J. Geophys. Res.*, *97*, 14841–14847.

Lockwood, M., Carlson, Jr., H. C., and Sandholt, P. E. (1993), Implications of the altitude of transient 630-nm dayside auroral emission, *J. Geophys. Res.*, *98*, 15571–15587.

Lu, G., Lyons, L. R., Reiff, P. H., Denig, W. F., de la Beaujardiere, O., Kroehl, H. W., Newell, P. T., Rich, F. J., Opgenoorth, H., Persson, M. A. L., Ruohoniemi, J. M., Friis-Christensen, E., Tomlinson, L., Morris, R., Burns, G., and McEwin, A. (1995), Characteristics of ionospheric convection and field-aligned current in the dayside cusp region, *J. Geophys. Res.*, *100*, 11845–11861.

Lu, G., Richmond, A. D., Ruohoniemi, J. M., Greenwald, R. A., Hairston, M., Rich, F. J., and Evans, D. S. (2001), An investigation of the influence of data and model inputs on assimilative mapping of ionospheric electrodynamics, *J. Geophys. Res.*, *106*, 417–433.

Meng, C.-I., Holzworth, R. H., and Akasofu, S.-I. (1977), Auroral circle - Delineating the poleward boundary of the quiet auroral belt, *J. Geophys. Res.*, *82*, 164–172.

Milan, S. E., Lester, M., Cowley, S. W. H., Oksavik, K., Brittnacher, M., Greenwald, R. A., Sofko, G., and Villain, J.-P. (2003), Variations in the polar cap area during two substorm cycles, *Ann. Geophys.*, *21*, 1121–1140.

Milan, S. E., Provan, G., and Hubert, B. (2007), Magnetic flux transport in the Dungey cycle: A survey of dayside and nightside reconnection rates, *J. Geophys. Res.*, *112*, A01209, doi:10.1029/2006JA011642.

Newell, P. T., Burke, W. J., Sanchez, E. R., Meng, C.-I., Greenspan, M. E., and Clauer, C. R. (1991), The low-latitude boundary layer and the boundary plasma sheet at low altitude: Prenoon precipitation regions and convection reversal boundaries, *J. Geophys. Res.*, *96*, 21013–21023.

Newell, P. T., and Meng, C.-I. (1992), Mapping the dayside ionosphere to the magnetosphere according to particle precipitation characteristics, *Geophys. Res. Lett.*, *19*, 609–612.

Newell, P. T., Feldstein, Y. I., Galperin, Y. I., and Meng, C.-I. (1996), Morphology of nightside precipitation, *J. Geophys. Res.*, *101*, 10737–10748.

Østgaard, N., Moen, J., Mende, S. B., Frey, H. U., Immel, T. J., Gallop, P., Oksavik, K., and Fujimoto, M. (2005), Estimates of magnetotail reconnection rate based on IMAGE FUV and EISCAT measurements, *Ann. Geophys.*, *23*, 123–134.

Phan, T. D., Kistler, L., Klecker, B., Haerendel, G., Paschmann, G., Sonnerup, B. U. O., Baumjohann, W., Bavassano-Cattaneo, M. B., Carlson, C. W., Dilellis, A. M., Fornacon, K. H., Frank, L. A., Fujimoto, M., Georgescu, E., Kokubun, S., Moebius, E.,Mukai, T., Oieroset, M., Paterson, W. R., and Reme, H. (2000), Extended magnetic reconnection at the Earth's magnetopause from detection of bi-directional jets, *Nature*, *404*, 848–850.

Phan, T. D., Gosling, J. T., Davis, M. S., Skoug, R. M., Øieroset, M., Lin, R. P., Lepping, R. P., McComas, D. J., Smith, C. W., Reme, H., and Balogh, A. (2006), A magnetic reconnection X-line extending more than 390 Earth radii in the solar wind, *Nature*, *439*, 175–178.

Pinnock, M., Rodger, A. S., Baker, K. B., Lu, G., and Hairston, M. (1999), Conjugate observations of the day-side reconnection electric field: A GEM boundary layer campaign, *Ann. Geophys.*, *17*, 443–454.

Pinnock, M., Chisham, G., Coleman, I. J., Freeman, M. P., Hairston, M., and Villain, J.-P. (2003), The location and rate of dayside reconnection during an interval of southward interplanetary magnetic field, *Ann. Geophys.*, *21*, 1467–1482.

Ponomarenko, P. V., and Waters, C. L. (2003), The role of Pc1-2 waves in spectral broadening of SuperDARN echoes from high latitudes, *Geophys. Res. Lett.*, *30*, 1122, doi:10.1029/2002GL016333.

Priest, E., and Forbes, T. (2000), *Magnetic reconnection: MHD theory and applications*, Cambridge University Press.

Provan, G., Yeoman, T. K., Milan, S. E., Ruohoniemi, J. M., and Barnes, R. (2002), An assessment of the "map-potential" and "beam-swinging" techniques for measuring the ionospheric convection pattern using data from the SuperDARN radars, *Ann. Geophys.*, *20*, 191–202.

Rees, M. H. (1963), Auroral ionization and excitation by incident energetic electrons, *Planet. Space Sci.*, *11*, 1209–1218.

Reiff, P. H., Spiro, R. W., and Hill, T. W. (1981), Dependence of polar cap potential drop on interplanetary parameters, *J. Geophys. Res.*, *86*, 7639–7648.

Reiff, P. H., and Burch, J. L. (1985), IMF B_y-dependent plasma flow and Birkeland currents in the dayside magnetosphere, 2, A global model for northward and southward IMF, *J. Geophys. Res.*, *90*, 1595–1609.

Richmond, A. D., and Kamide, Y. (1988), Mapping electrodynamic features of the high-latitude ionosphere from localized observations: Technique, *J. Geophys. Res.*, *93*, 5741–5759.

Rodger, A. S. (2000), Ground-based ionospheric imaging of magnetospheric boundaries, *Adv. Space Res.*, *25*, (7/8)1461–1470.

Rodger, A. S., and Pinnock, M. (1997), The ionospheric response to flux transfer events: The first few minutes, *Ann. Geophys.*, *15*, 685–691.

Rosenbauer, H., Gruenwaldt, H., Montgomery, M. D., Paschmann, G., and Sckopke, N. (1975), HEOS 2 plasma observations in the distant polar magnetosphere: the plasma mantle, *J. Geophys. Res.*, *80*, 2723–2737.

Ruohoniemi, J. M., and Greenwald, R. A. (1996), Statistical patterns of high-latitude convection obtained from Goose Bay HF radar observations, *J. Geophys. Res.*, *101*, 21743–21763.

Ruohoniemi, J. M., and Baker, K. B. (1998), Large-scale imaging of high-latitude convection with Super Dual Auroral Radar Network HF radar observations, *J. Geophys. Res.*, *103*, 20797–20811.

Ruohoniemi, J. M., Greenwald, R. A., Baker, K. B., Villain, J.-P., Hanuise, C., and Kelly, J. (1989), Mapping high-latitude plasma convection with coherent HF radars, *J. Geophys. Res.*, *94*, 13463–13477.

Russell, C. T. (1972), The configuration of the magnetosphere, in *Critical Problems of Magnetospheric Physics*, edited by E. R. Dyer, pp. 1–16, Inter-Union Commission on Solar-Terrestrial Physics Secratariat, National Academy of Sciences, Washington, D.C.

Russell, C. T., and Elphic, R. C. (1978), Initial ISEE magnetometer results: Magnetopause observations, *Space Sci. Rev.*, *22*, 681–715.

Shepherd, S. G., and Ruohoniemi, J. M. (2000), Electrostatic potential patterns in the high-latitude ionosphere constrained by SuperDARN measurements, *J. Geophys. Res.*, *105*, 23005–23014.

Siscoe, G. L., and Huang, T. S. (1985), Polar cap inflation and deflation, *J. Geophys. Res.*, *90*, 543-547.

Sonnerup, B. U. Ö., Paschmann, G., Papamastorakis, I., Sckopke, N., Haerendel, G., Bame, S. J., Asbridge, J. R., Gosling, J. T., and Russell, C. T. (1981), Evidence for magnetic field reconnection at the Earth's magnetopause, *J. Geophys. Res.*, *86*, 10049–10067.

Sotirelis, T., and Newell, P. T. (2000), Boundary-oriented electron precipitation model, *J. Geophys. Res.*, *105*, 18655–18673.

Sotirelis, T., Ruohoniemi, J. M., Barnes, R. J., Newell, P. T., Greenwald, R. A., Skura, J. P., and Meng, C.-I. (2005), Comparison of SuperDARN radar boundaries with DMSP particle precipitation boundaries, *J. Geophys. Res.*, *110*, A06302, doi:10.1029/2004JA010732.

Taylor, J. R., Yeoman, T. K., Lester, M., Emery, B. A., and Knipp, D. J. (1996), Variations in the polar cap area during intervals of substorm activity on 20–21 March 1990 deduced from AMIE convection patterns, *Ann. Geophys.*, *14*, 879–887.

Torr, M. R., Torr, D. G., Zukic, M., Johnson, R. B., Ajello, J., Banks, P., Clark, K., Cole, K., Keffer, C., Parks, G., Tsurutani, B., and Spann, J. (1995), A far ultraviolet imager for the international solar-terrestrial physics mission, *Space Sci. Rev.*, *71*, 329–383.

Tsyganenko, N. A. (1995), Modelling the Earth's magnetospheric magnetic field confined within a realistic magnetopause, *J. Geophys. Res.*, *100*, 5599–5612.

Tsyganenko, N. A., and Stern, D. P. (1996), Modelling the global magnetic field of large-scale Birkeland current systems, *J. Geophys. Res.*, *101*, 27187–27198.

Vasyliunas, V. M. (1984), Steady state aspects of magnetic field line merging, in *Magnetic Reconnection in Space and Laboratory Plasmas, Geophys. Monogr. Ser.*, vol 30, edited by E. W. Hones Jr., p. 25, AGU, Washington, D.C.

Wild, J. A., Milan, S. E., Owen, C. J., Bosqued, J. M., Lester, M., Wright, D. M., Frey, H., Carlson, C. W., Fazakerley, A. N., and Rème, H. (2004), The location of the open-closed magnetic field line boundary in the dawn sector auroral ionosphere, *Ann. Geophys.*, *22*, 3625–3639.

Figure 1. A 2-dimensional schematic representation of a reconnection X-line. The black lines portray the magnetic field configuration around the neutral point. The blue arrows illustrate the plasma inflow into, and outflow from, the neutral point. The current flow (green) is shown as being directed out of the page. (taken from http://en.wikipedia.org/wiki/Image:Reconnection_Illustrations.png)

Figure 2. A 2-dimensional schematic representation of the magnetosphere as shown in the noon-midnight meridian plane during an interval of southward-directed interplanetary magnetic field. The black lines represent the Earth's magnetic field. The neutral points at the points labelled N_1 and N_2 highlight the locations of magnetopause (dayside) and magnetotail (nightside) reconnection for these conditions. (taken from http://en.wikipedia.org/wiki/Image:Substorm.jpg)

Figure 3. A 3-dimensional schematic representation illustrating the reconnection separatrix (yellow and green shaded regions). The separatrix extends from the magnetopause and magnetotail X-lines (bold blue lines in space), down converging magnetic field lines (red lines) into the ionosphere. The ionospheric projections of the reconnection separatrix are termed the merging lines (bold blue lines in the ionosphere). In the pictured scenario the interplanetary magnetic field is assumed to be in a southward direction and in this case the reconnection separatrix is co-located with the open-closed magnetic field line boundary.

Figure 4. Schematic diagrams of the measurement scenario at a longitude ϕ_i, (a) showing the measured quantities, velocity vector V_i located at (λ_i, ϕ_i) and reconnection separatrix $\mathbf{P}(t)$, (b) showing the derived quantities, α_i, θ_i, and $V_{\mathbf{P}_i}$ at separatrix location $\mathbf{P}_i$.

Figure 5. A northern hemisphere SuperDARN global convection map from 2017 UT on 26 December 2000. The vectors are 'true' vectors with a length proportional to the velocity magnitude. The dashed (morning cell) and dotted (afternoon cell) lines illustrate the convection electric potential solution at this time.

Figure 6. A Polar UVI image of the northern hemisphere auroral oval measured at 2017:34 UT on 26 December 2000. The black symbols represent the poleward edge of the auroral oval as estimated using the method of *Carbary et al.* [2003]. The red symbols represent these estimates corrected to provide the best estimates for the OCB using the corrections of *Carbary et al.* [2003]. The radial blue lines highlight the MLT sectors for which latitudinal auroral intensity profiles are presented in fig.7.

Figure 7. Latitudinal auroral intensity profiles (solid histograms), taken from the Polar UVI auroral image presented in fig.6 in three MLT sectors. The dotted lines illustrate the *Carbary et al.* [2003] fits to the latitudinal profiles and the vertical dashed line highlights the poleward edge as determined using the *Carbary et al.* [2003] algorithm.

Figure 8. The Doppler spectral width measured by beams 7-14 of the Kapuskasing SuperDARN radar at 2017 UT on 26 December 2000. (a) The raw spectral width data, (b) the spatially and temporally median-filtered spectral width data, and (c) the proportion of the filtered data set that was >150 m/s (black). The dashed line represents the 1500 MLT meridian. The white squares in (c) highlight the locations of spectral width boundaries that were determined in this data.

Figure 9. An example of using a truncated Fourier series to describe the OCB (at 2017-2018 UT on 26 December 2000). The squares represent UVI boundary measurements made between 2016 and 2019 UT and the diamonds represent SWBs measured by the Kapuskasing, Kodiak, and Prince George SuperDARN radars during the same interval. The solid (dotted) line represents a 10th (6th) order Fourier series.

Figure 10. (a) The distribution of Polar UVI boundary velocity in the 2000-2200 UT interval on 26 December 2000 determined from temporally adjacent samples (solid line), at a temporal spacing of 2 samples (dashed line), and at a temporal spacing of 4 samples (dotted line). (b) The distribution of Polar UVI boundary velocity for the same interval determined from the temporally-filtered UVI observations (solid line), and the distributions of boundary velocity for the 6th order (dashed line) and 10th order (dotted line) Fourier series representations of the OCB.

Figure 11. A time series of polar plots showing the development of the OCB and the polar cap over the interval 2000-2200 UT on 26 December 2000. Each frame shows the fitted OCB (bold line) and the raw Polar UVI and SWB boundaries used to determine the OCB (squares). The frames represent a 1-min interval separated every 10 min.

Figure 12. A combination of the convection map presented in fig.5 with the OCB estimate presented in fig.9 (bold line). The grey shaded regions highlight velocity vectors located close to the OCB that are used to determine the reconnection rate.

Figure 13. The spatial variation of the reconnection rate (with MLT). (a) The variation of the total reconnection rate. The bold black line and grey shaded region represent the variation of the mean and standard deviation of the reconnection rate measurements determined in a 2-hour MLT sliding window. (b) The contribution to the total reconnection rate that comes from measurements of the plasma flow. (c) The contribution to the total reconnection rate that comes from the boundary motion.

Figure 14. (a) The temporal variation in IMF B_y (bold line) and IMF B_z (solid line) as measured by the ACE spacecraft, shifted by 63 min to account for the solar wind propagation from ACE. (b) The IMF clock angle measured by ACE, shifted by 63 min to account for the solar wind propagation from ACE. (c) The polar cap area variation estimated from the global OCB determinations. (d) The average dayside reconnection rate (black line). The white line represents the mean measurement determined in a 15-min sliding window. (e) The average nightside reconnection rate (black line). The white line represents the mean measurement determined in a 15-min sliding window. The two vertical dashed lines represent the estimated times of a substorm onset and a substorm intensification.

Figure 15. A comparison of the measured variation in polar cap area (solid line) with that predicted by the measured reconnection rate variations (dashed line), assuming certain dayside and nightside merging line lengths. (a) Assuming fixed merging line lengths for the whole 2-hour interval. (b) Assuming different merging line lengths in three different time periods within the interval. The assumed merging line lengths for the dayside and nightside are displayed on the figure as L_d and L_n respectively.

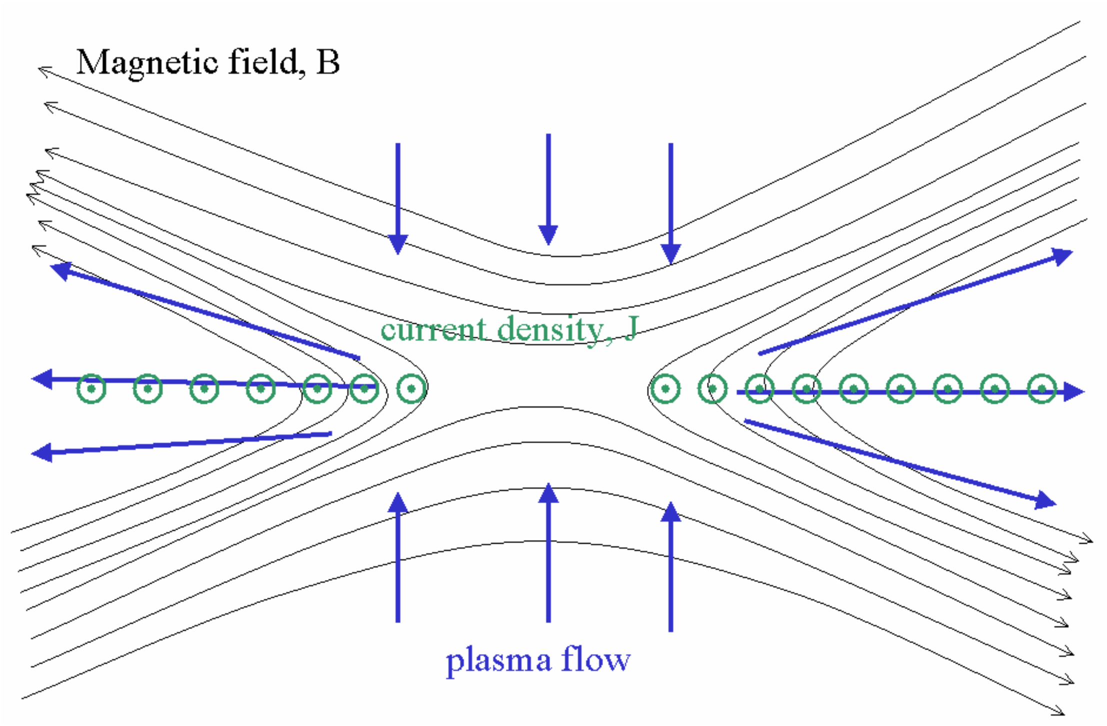

Figure 1

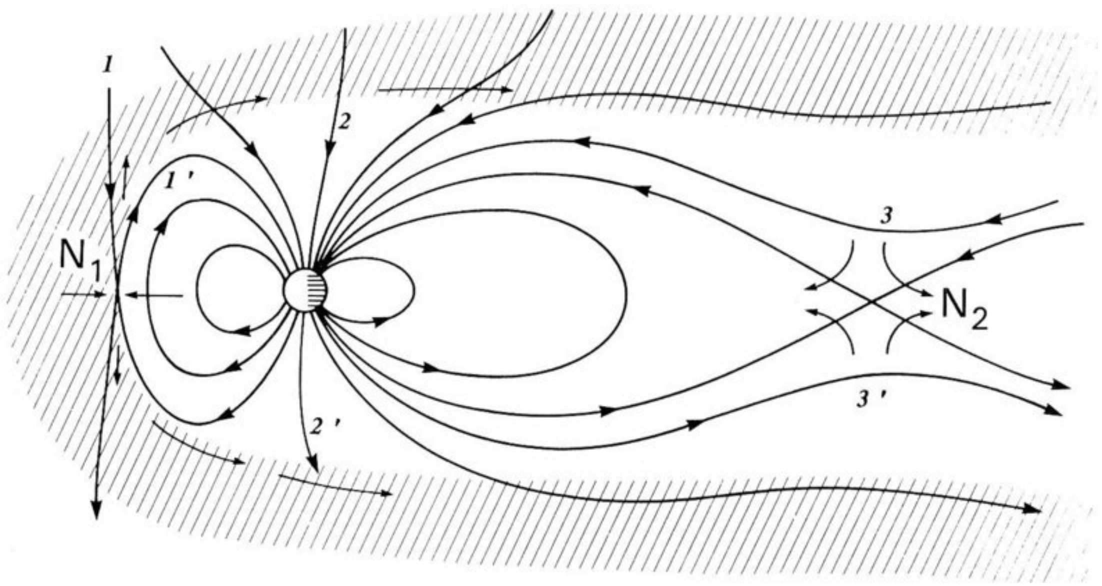

Figure 2

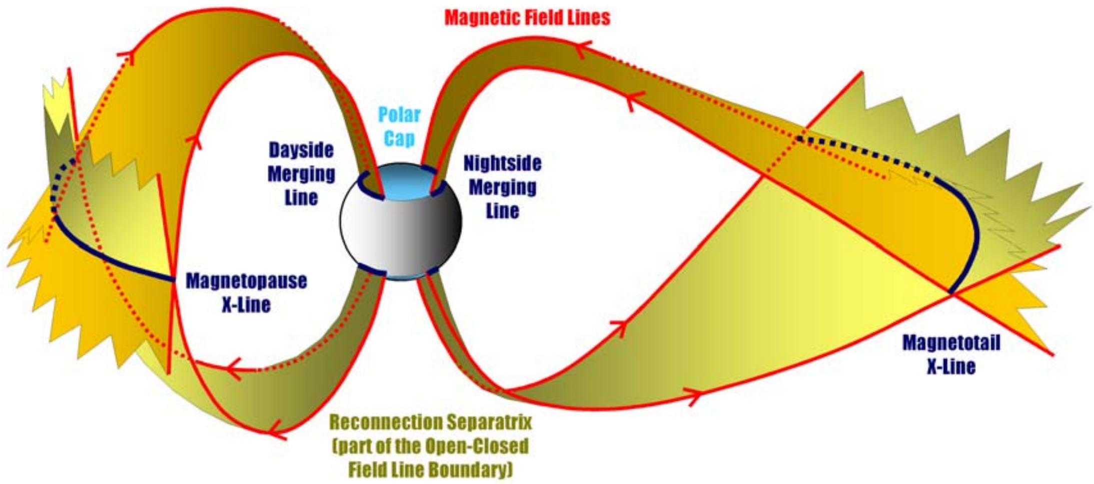
Magnetic Field Lines
Polar
Cap
Dayside
Merging
Line
Nightside
Merging
Line
Magnetopause
X-Line
Magnetotail
X-Line
Reconnection Separatrix
(part of the Open-Closed
Field Line Boundary)

Figure 3

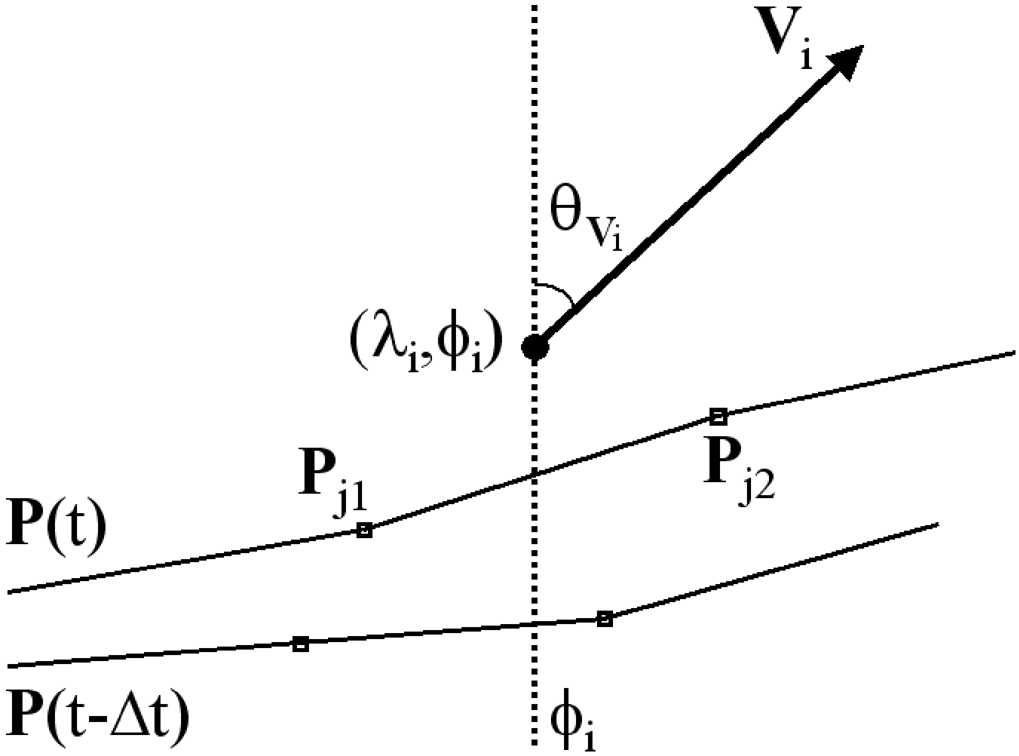

Figure 4a

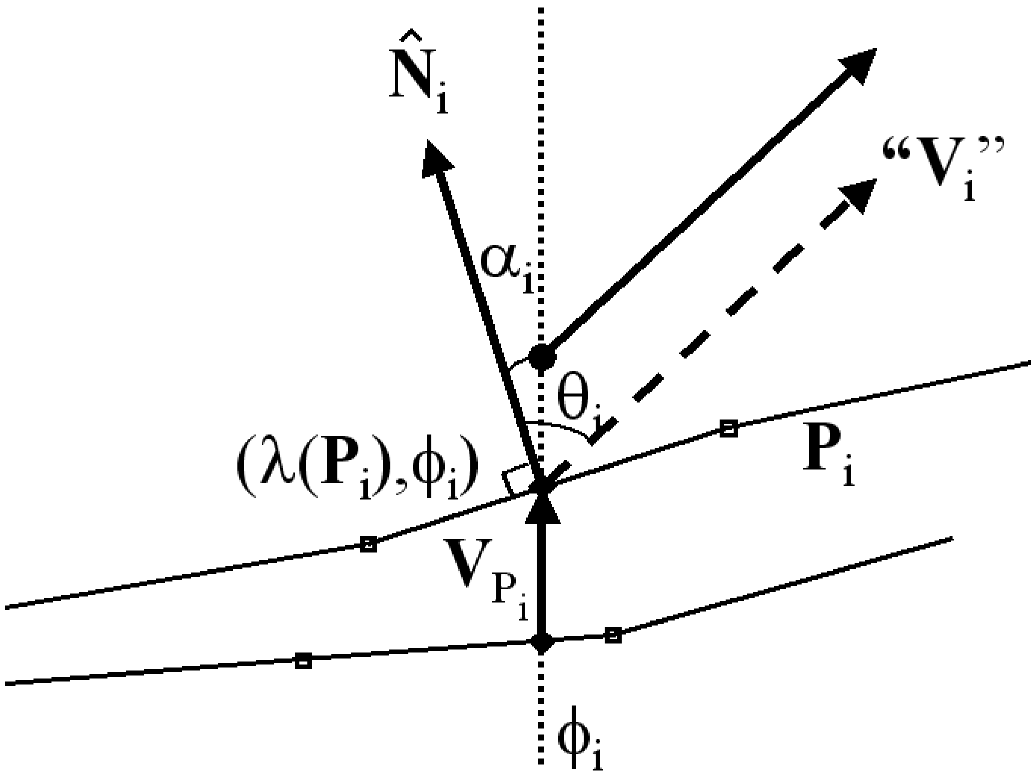

Figure 4b

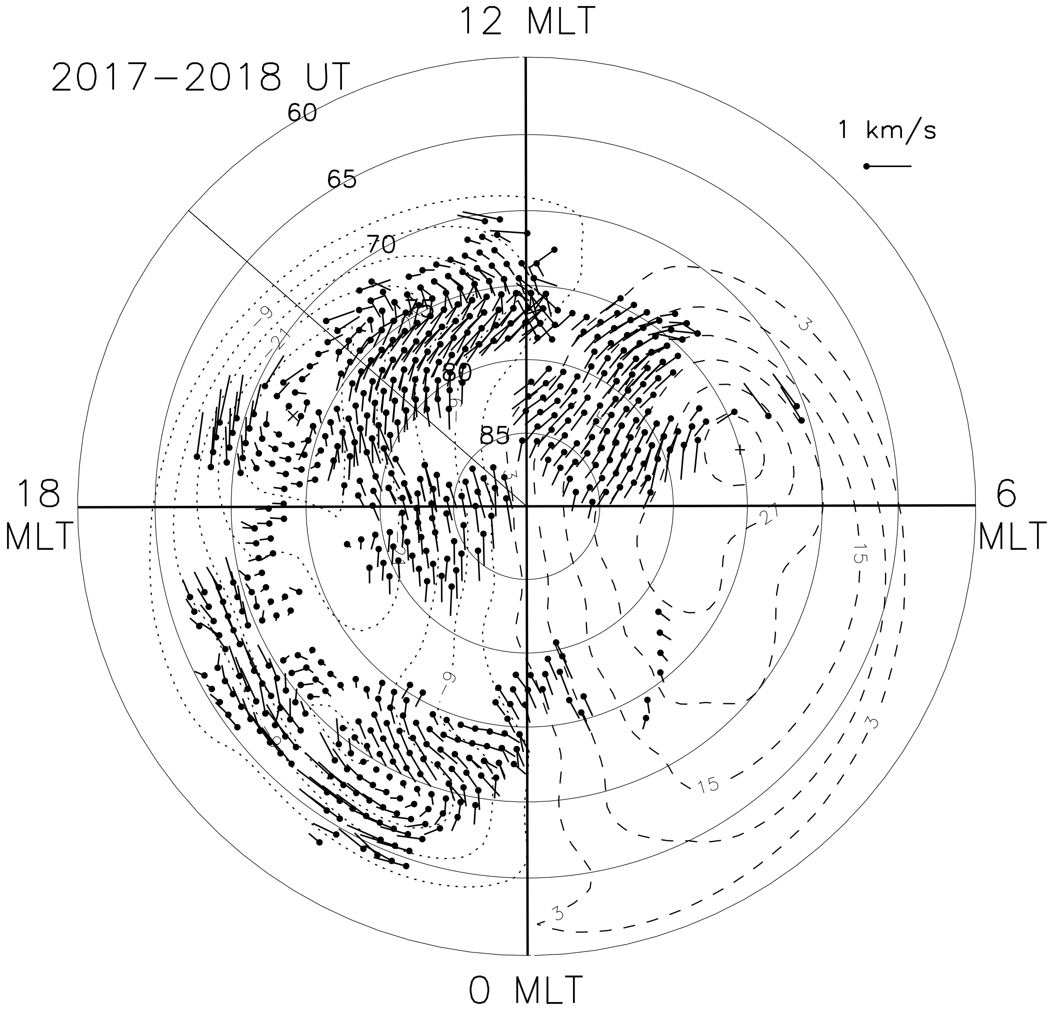

Figure 5

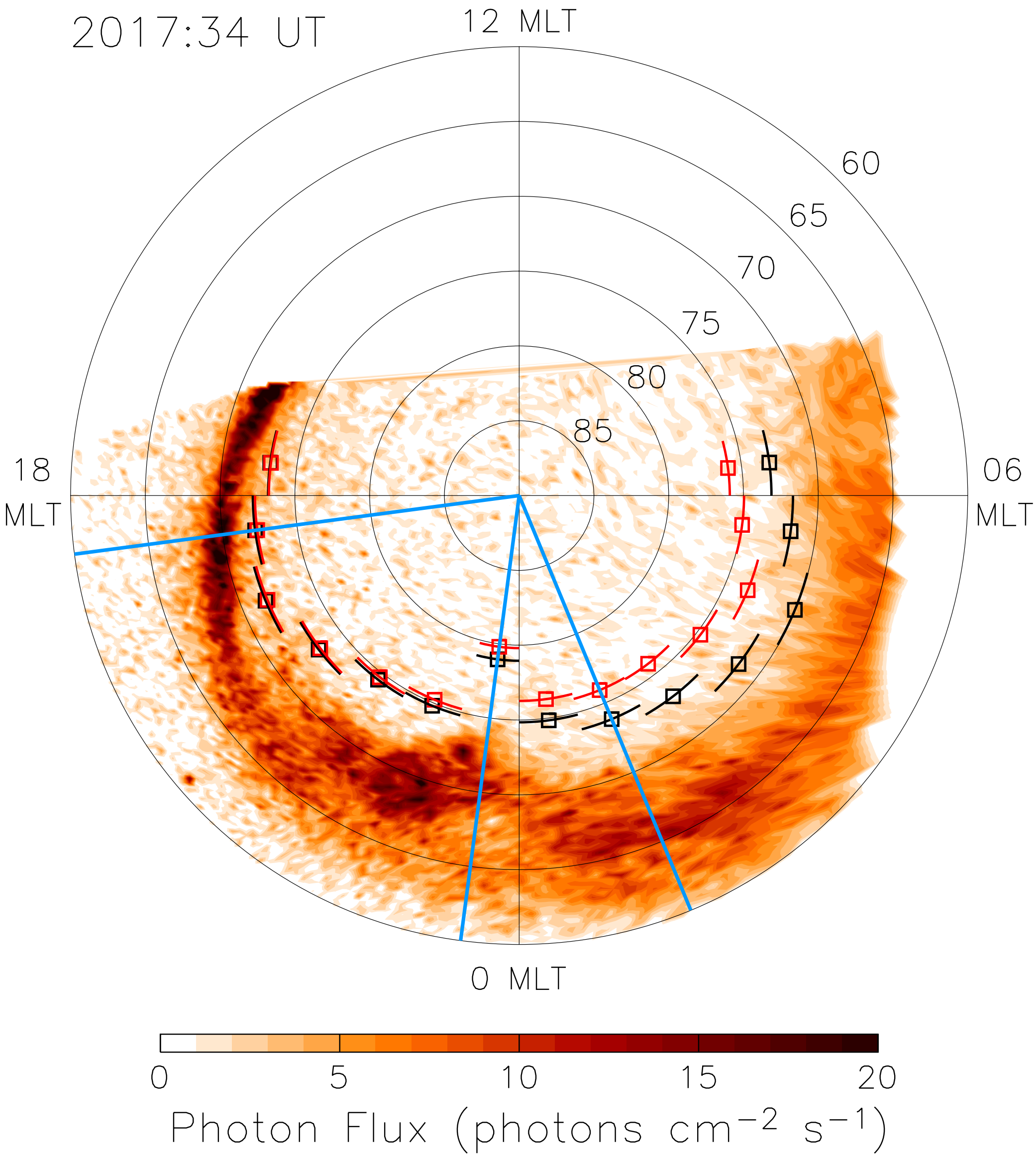

2017:34 UT
12 MLT
60
65
70
75
80
85
18
MLT
06
MLT
0 MLT
0
5
10
15
20
Photon Flux (photons cm^{-2} s^{-1})

Figure 6

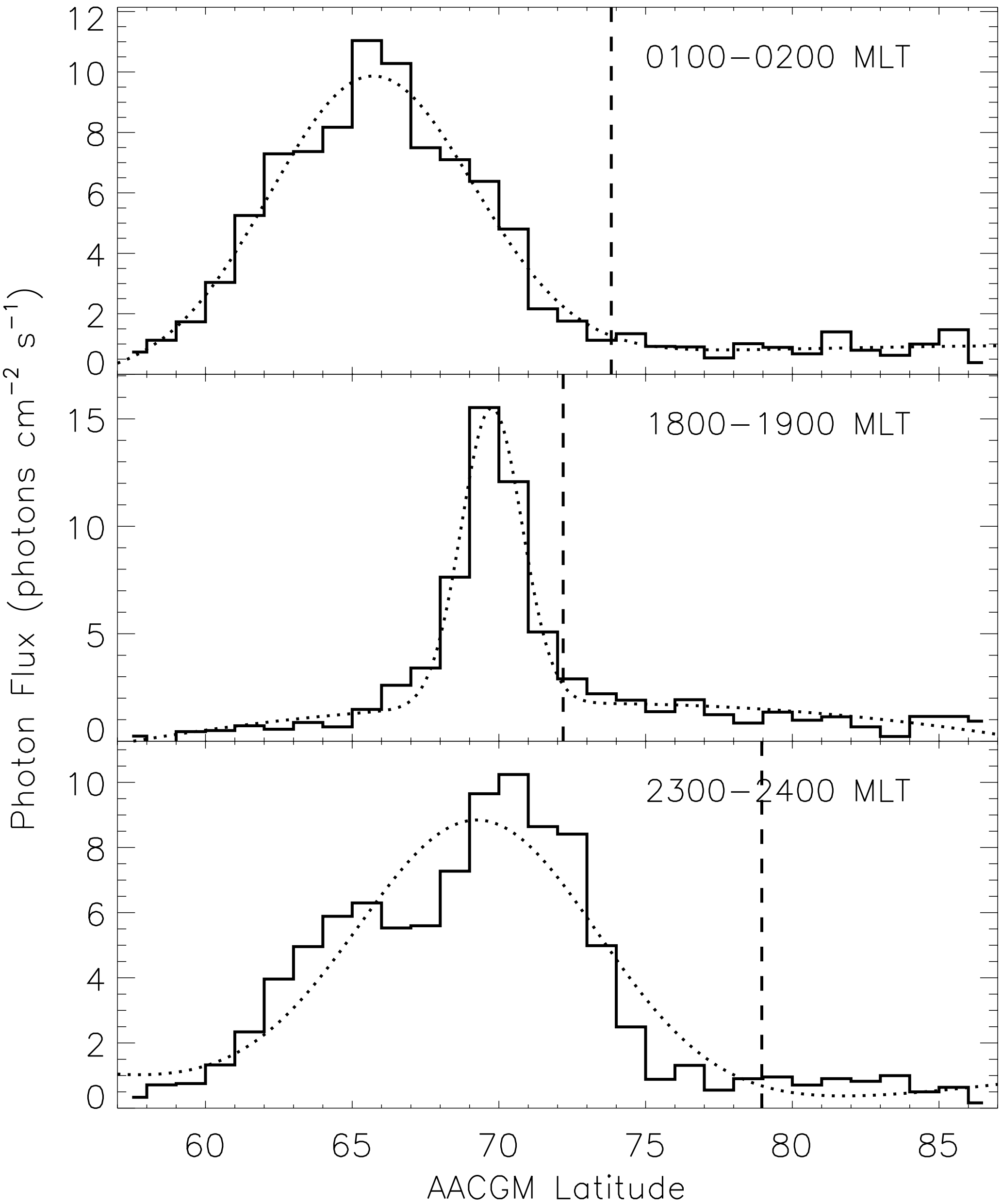
0100–0200 MLT
1800–1900 MLT
2300–2400 MLT
Photon Flux (photons cm^{-2} s^{-1})
AACGM Latitude
0
2
4
6
8
10
12
5
15
60
65
70
75
80
85

Figure 7

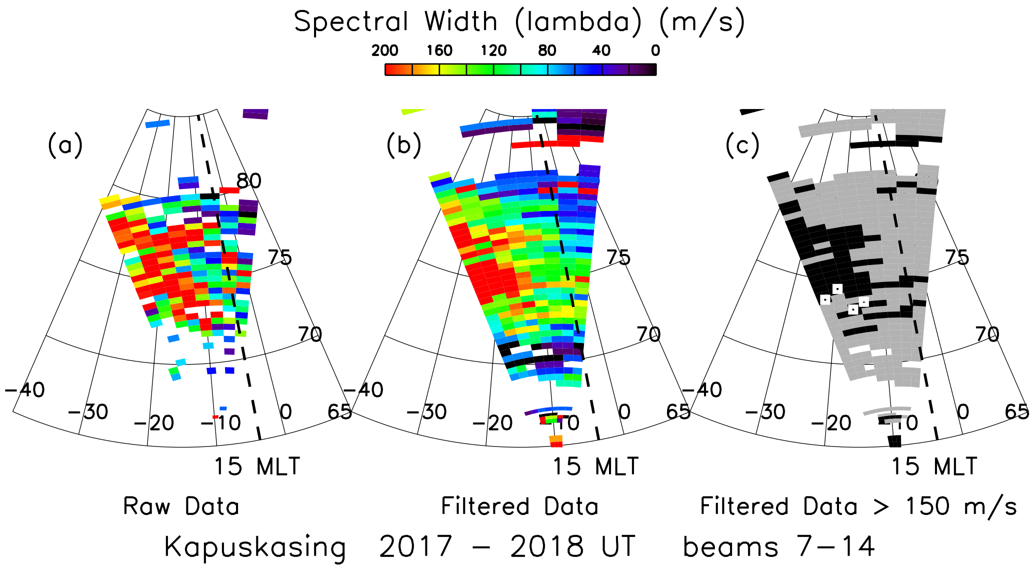

Spectral Width (lambda) (m/s)
200 160 120 80 40 0
(a)
(b)
(c)
80
75
70
65
−40
−30
−20
−10
0
15 MLT
Raw Data
Filtered Data
Filtered Data > 150 m/s
Kapuskasing 2017 − 2018 UT beams 7−14

Figure 8

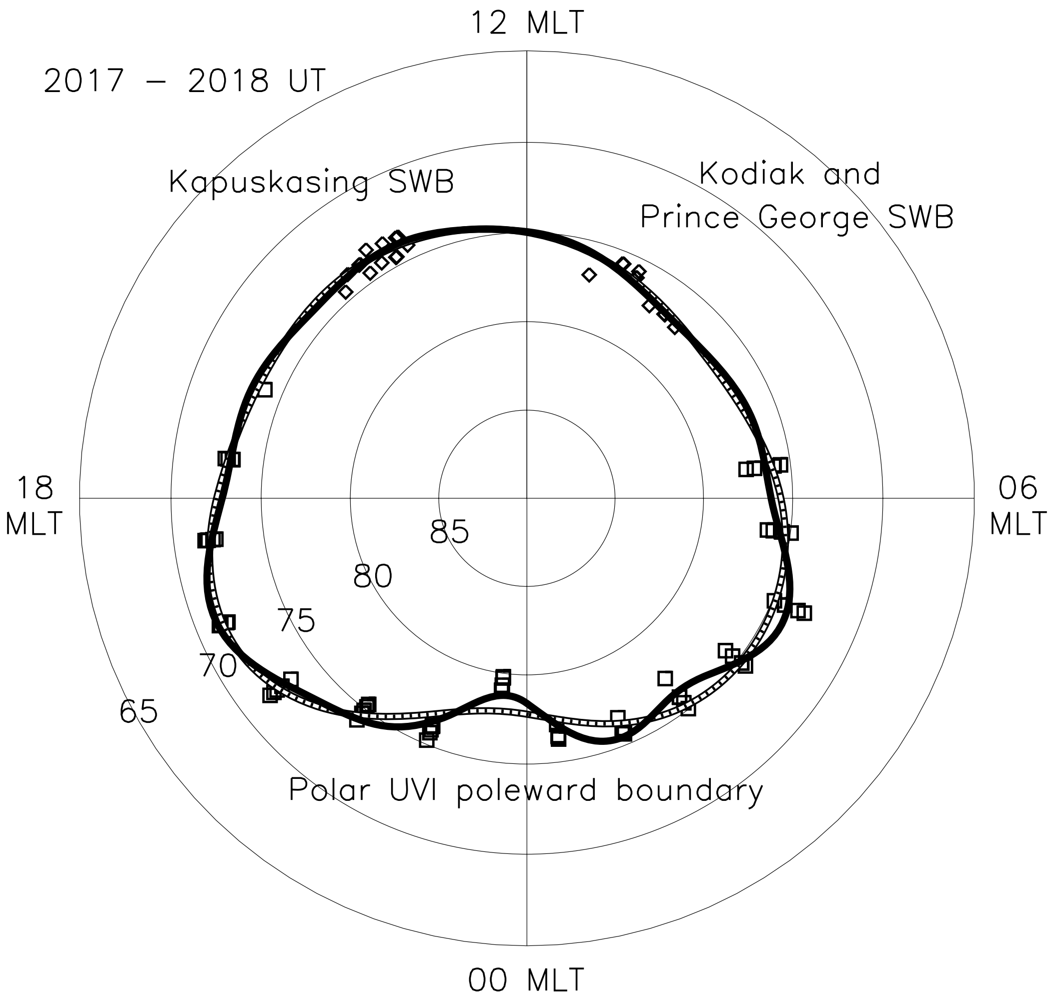
12 MLT
2017 – 2018 UT
Kapuskasing SWB
Kodiak and
Prince George SWB
18
MLT
06
MLT
85
80
75
70
65
Polar UVI poleward boundary
00 MLT

Figure 9

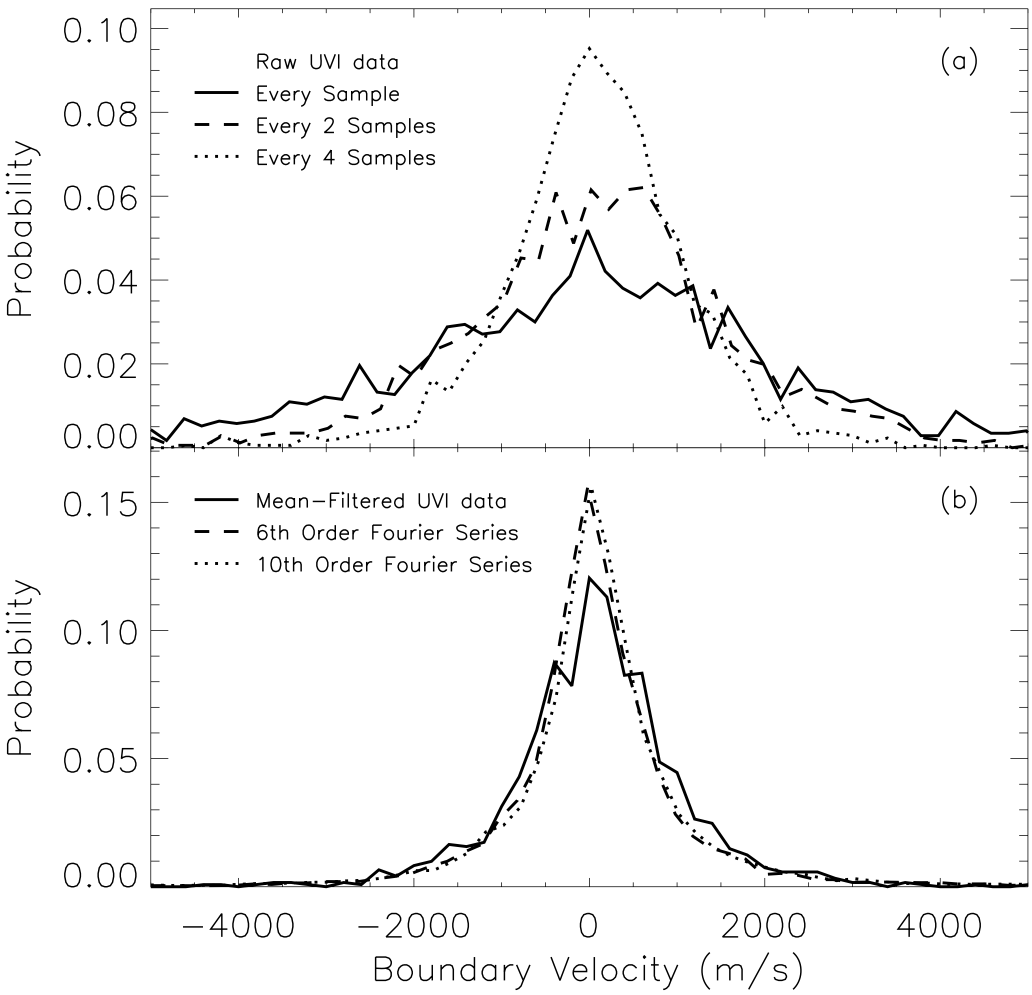

Probability
(a)
Raw UVI data
Every Sample
Every 2 Samples
Every 4 Samples
0.10
0.08
0.06
0.04
0.02
0.00
(b)
Mean-Filtered UVI data
6th Order Fourier Series
10th Order Fourier Series
0.15
0.10
0.05
0.00
−4000
−2000
0
2000
4000
Boundary Velocity (m/s)

Figure 10

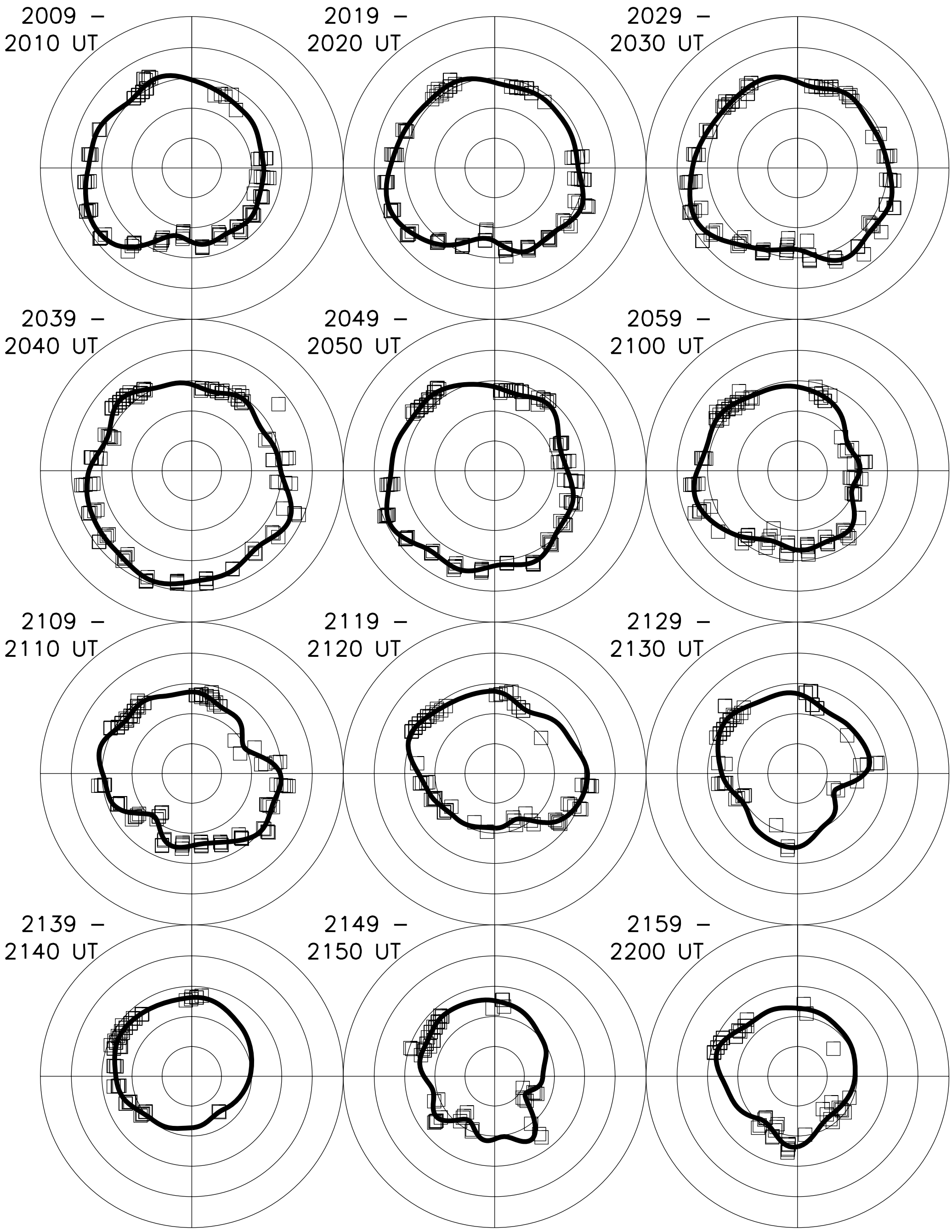
2009 –
2010 UT
2019 –
2020 UT
2029 –
2030 UT
2039 –
2040 UT
2049 –
2050 UT
2059 –
2100 UT
2109 –
2110 UT
2119 –
2120 UT
2129 –
2130 UT
2139 –
2140 UT
2149 –
2150 UT
2159 –
2200 UT

Figure 11

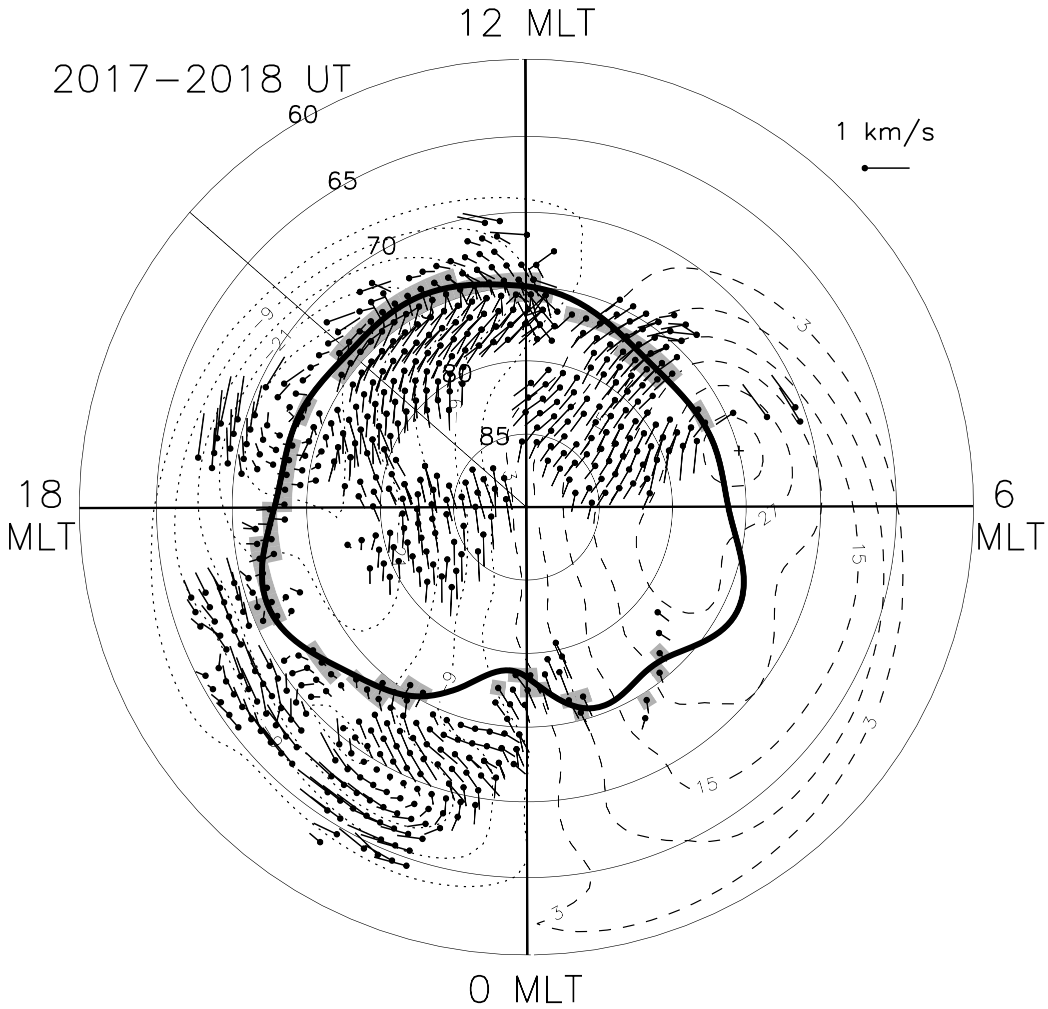
12 MLT
2017–2018 UT
1 km/s
60
65
70
80
85
18
MLT
6
MLT
0 MLT
-9
-21
3
-3
27
15
3
9
15
-3

Figure 12

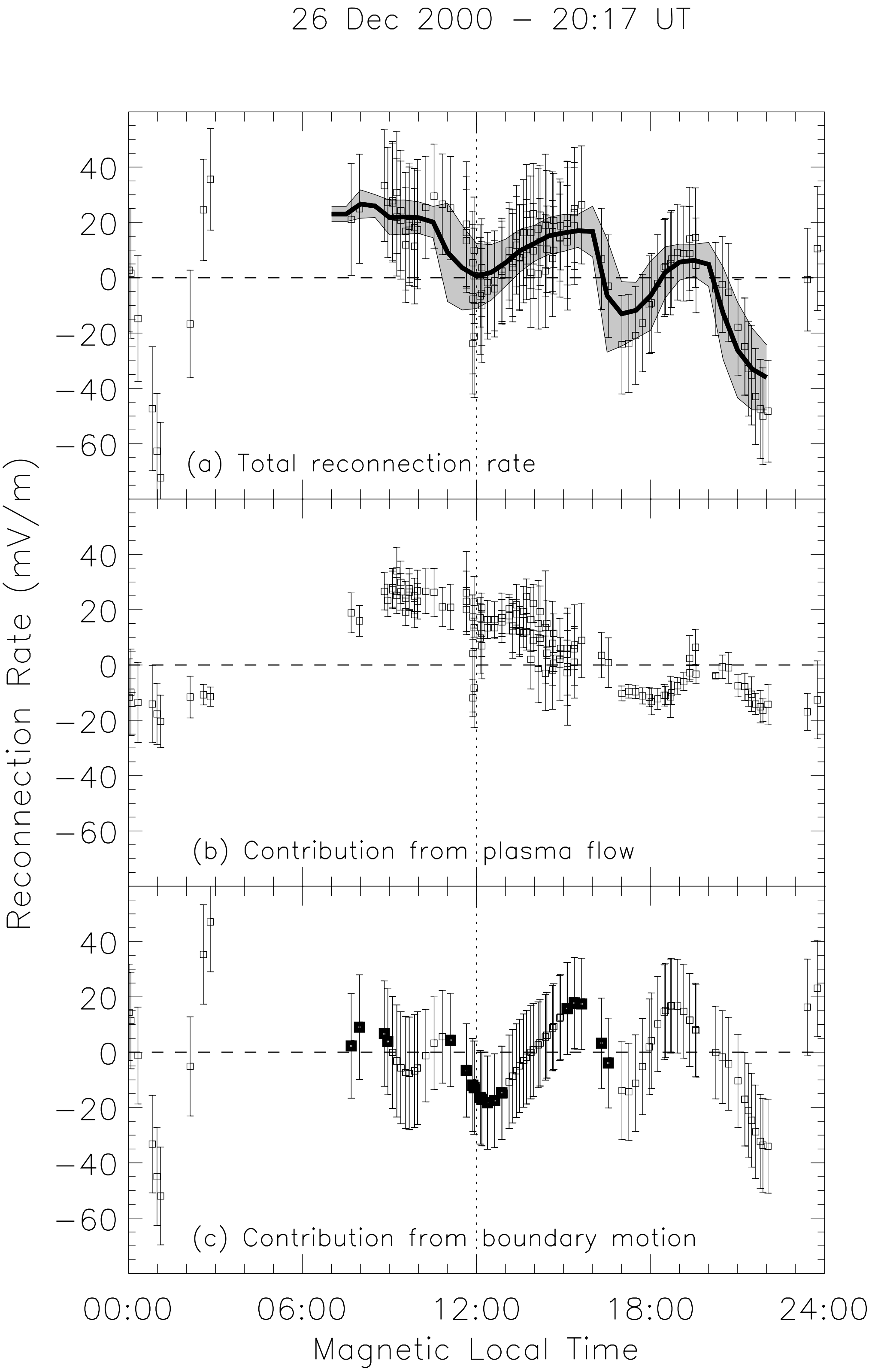
26 Dec 2000 – 20:17 UT
Reconnection Rate (mV/m)
(a) Total reconnection rate
(b) Contribution from plasma flow
(c) Contribution from boundary motion
40
20
0
−20
−40
−60
00:00
06:00
12:00
18:00
24:00
Magnetic Local Time

Figure 13

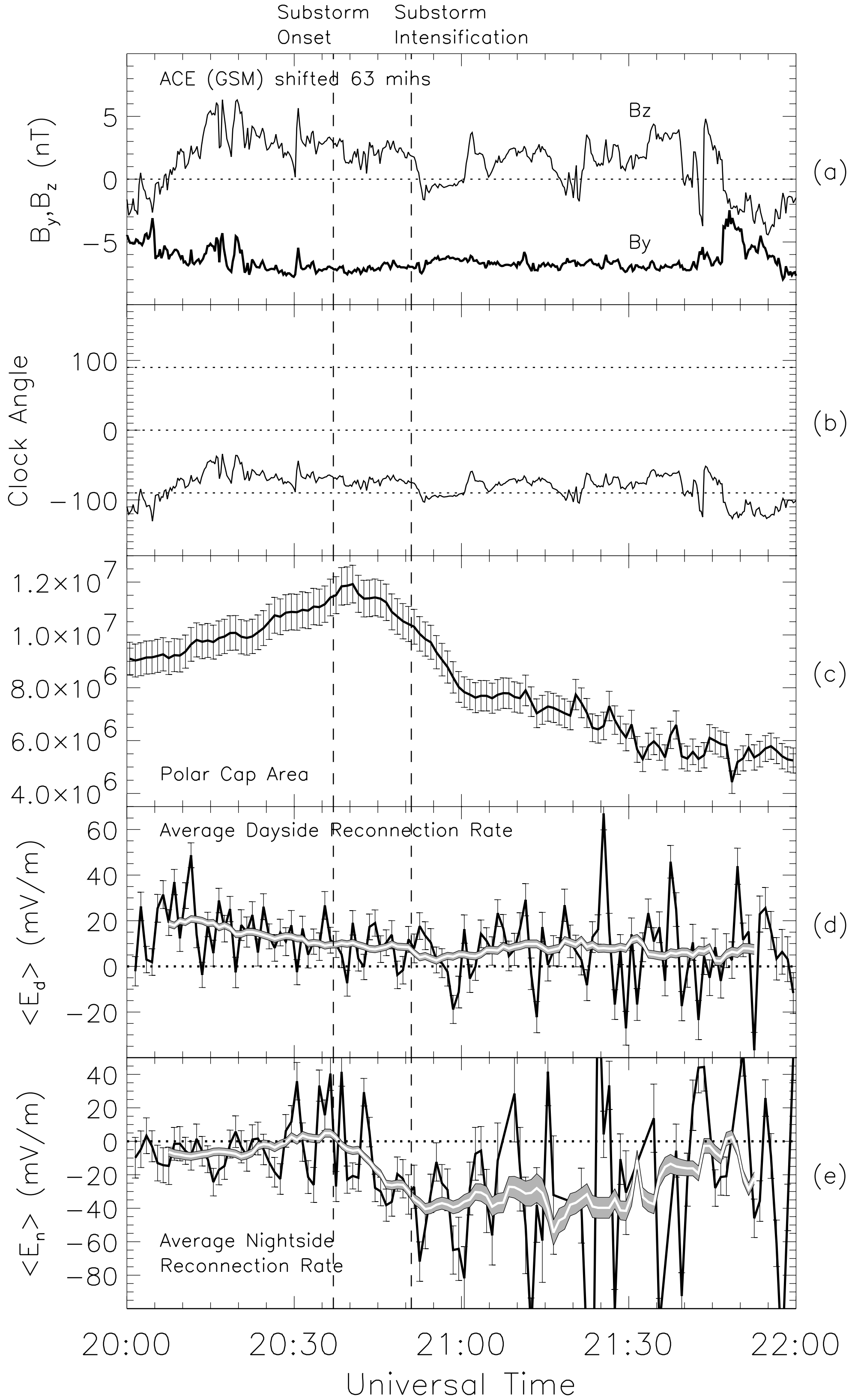

Substorm
Onset
Substorm
Intensification
ACE (GSM) shifted 63 mins
Bz
By
B_y, B_z (nT)
(a)
Clock Angle
(b)
A (km²)
Polar Cap Area
(c)
Average Dayside Reconnection Rate
$<E_d>$ (mV/m)
(d)
$<E_n>$ (mV/m)
Average Nightside
Reconnection Rate
(e)
20:00
20:30
21:00
21:30
22:00
Universal Time

Figure 14

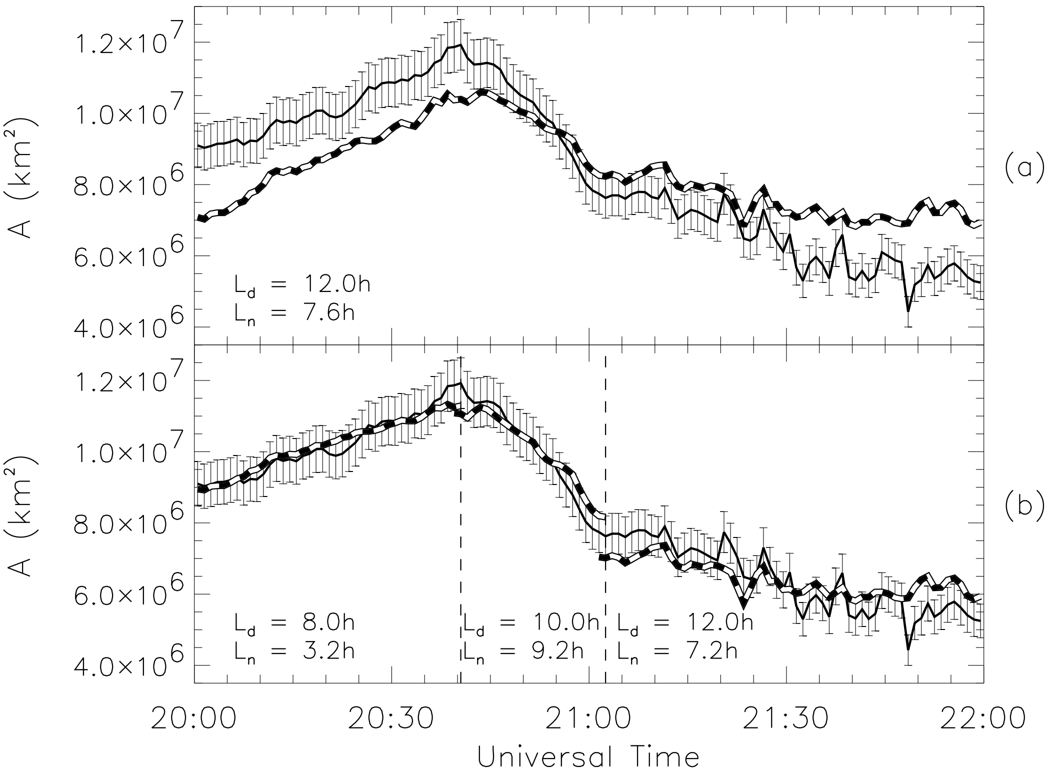

1.2×10^7
1.0×10^7
8.0×10^6
6.0×10^6
4.0×10^6
A (km²)
(a)
L_d = 12.0h
L_n = 7.6h
(b)
L_d = 8.0h
L_n = 3.2h
L_d = 10.0h
L_n = 9.2h
L_d = 12.0h
L_n = 7.2h
20:00
20:30
21:00
21:30
22:00
Universal Time

Figure 15